5-2016

Effects of Radiation Heating on Additively Printed Hybrid Fuel Grain Oxidizer-to-fuel Ratio Shift

Stephen L. Merkley
Utah State University

Recommended Citation

Merkley, Stephen L., "Effects of Radiation Heating on Additively Printed Hybrid Fuel Grain Oxidizer-to-fuel Ratio Shift" (2016). *All Graduate Theses and Dissertations*. 5230.
https://digitalcommons.usu.edu/etd/5230

EFFECTS OF RADIATION HEATING ON ADDITIVELY PRINTED HYBRID FUEL GRAIN OXIDIZER-TO-FUEL RATIO SHIFT

by

Stephen L. Merkley

A thesis submitted in partial fulfillment
of the requirements for the degree

of

MASTER OF SCIENCE

in

Aerospace Engineering

Approved:

Stephen Whitmore, Ph.D. Major Professor	Rees Fullmer, Ph.D. Committee Member
David Geller, Ph.D. Committee Member	Mark McLellan, Ph.D. Vice President for Research and Dean of the School of Graduate Studies

UTAH STATE UNIVERSITY
Logan, Utah

2016

ABSTRACT

Effects of Radiation Heating on Additively Printed Hybrid Fuel
Grain Oxidizer-to-Fuel Ratio Shift

by

Stephen L. Merkley, Master of Science

Utah State University, 2016

Major Professor: Dr. Stephen A. Whitmore
Department: Mechanical and Aerospace Engineering

Utah State University has researched and developed a hybrid rocket system that uses a non-toxic, simple, and 3D-printed plastic as the fuel. This plastic is ABS (acrylonitrile butadiene styrene), which is a common material used in pipe systems, automotive components, and toys such as Lego bricks. As a fuel, additively-printed ABS has structural properties that outweigh other polymer fuels, has matching or better performance than most commonly used propellants, is an environmentally-friendly fuel, is easily manufactured and assembled, and has allowed for very small-scale hybrid motors to be feasible. However, the performance of printed ABS is inaccurately predicted by current ballistics models since the oxidizer-to-fuel (O/F) ratio becomes more fuel-rich with time – contrary to most hybrid rocket motor (HRM) propellants, which become increasingly oxidizer-rich with time. The cause is hypothesized to be a normally negligible radiative energy transfer mechanism, which becomes more significant in smaller-scale motor systems, as well as fuel/oxidizer combinations that have lower stoichiometric O/F ratios. As such, an entirely new regime of mass flux is encountered, where the burn behavior is governed by a more extensive set of combustion physics. This study derives and tests a new fuel regression rate model that accounts for radiative energy transfer.

(73 pages)

PUBLIC ABSTRACT

Effects of Radiation Heating on Additively Printed Hybrid Fuel Grain Oxidizer-to-Fuel Ratio Shift

Stephen L. Merkley

This thesis examined the hypothesis that radiative heat transfer in small-scale printed-fuel hybrid rocket motors is responsible for the observed decreasing oxidizer-to-fuel (O/F) ratio shift. The magnitude of the radiation term was negligible for the motor sizes and types of propellants that have been previously tested, but was reintroduced in this study. To prove this hypothesis, a detailed enthalpy balance model was developed and tested using experimental fuel regression rate data obtained from a variety of motor scales using additively-manufactured acrylonitrile butadiene styrene (ABS) fuel grains.

ACKNOWLEDGMENTS

I would like to thank Dr. Stephen Whitmore for his guidance and I give thanks to my family, friends, and colleagues for their encouragement, suggestions, and moral support.

Stephen L. Merkley

CONTENTS

Page

CHAPTER

LIST OF TABLES

Table Page

LIST OF FIGURES

ACRONYMS

ABS	acrylonitrile butadiene styrene
CAD	computer-aided design
CEA	Chemical Equilibrium with Applications
CNC	computer numerically controlled
FDM	fused deposition modeling
GOX	gaseous oxygen
HDPE	high density polyethylene
HRM	hybrid rocket motor
HTPB	hydroxyl-terminated polybutadiene
IADC	Inter-Agency Space Debris Coordination Committee
L/D	length-to-diameter
LEO	low earth orbit
N_2O	nitrous oxide
O/F	oxidizer-to-fuel
RMSE	root mean squared error
TRL	technology readiness level
USU	Utah State University

NOMENCLATURE

$\dot{m}_f$	Fuel Mass Flow Rate
$\dot{m}_{ox}$	Oxidizer Mass Flow Rate
$\dot{q}_c$	Heat Flux Density Due to Convection
$\dot{q}_f$	Heat Flux Density Due to Ablated Fuel
$\dot{q}_r$	Heat Flux Density Due to Radiation
A_b	Burn Surface Area
A_c	Port Cross-sectional Area
A_i	Oxidizer Injector Area
A_t	Nozzle Throat Area
C_{f_B}	Skin Friction Coefficient with Radial Wall Blowing
c^*	Characteristic Velocity
C_f	Local Skin Friction Coefficient
c_p	Specific Heat at Constant Pressure of Combustion Product
G_f	Fuel Mass Flux
G_{ox}	Oxidizer Mass Flux
h_v	Fuel Enthalpy of Vaporization (Latent Heat)
I_{sp}	Specific Impulse
m_f	Fuel Mass
m_{ox}	Oxidizer Mass
P_0	Combustion Chamber Pressure
P_{ox}	Oxidizer Injector Pressure
P_r	Non-Dimensional Turbulent Prandtl Number
R_e	Reynolds Number
R_g	Specific Gas Constant
$\dot{r}$	Mean Longitudinal Fuel Regression Rate
S_t	Non-Dimensional Stanton Number
T_0	Combustion Flame Temperature
T_f	Fuel Temperature
U_e	Velocity of Combustion Product
U_{ox}	Velocity of Oxidizer

U_{wall}	Velocity of Boundary Layer Product
V_c	Combustion Chamber Volume
γ_{ox}	Oxidizer Specific Heat Ratio
ρ_e	Density of Combustion Product
ρ_f	Fuel Density
ρ_{ox}	Density of Oxidizer
ρ_{ox}	Oxidizer Density
ρ_{wall}	Density of Boundary Layer Product
σ_B	Stefan Boltzmann Constant
a	Regression Rate Model Scale Factor
D	Port Diameter
G	Total Mass Flux
j	Iteration
L	Port Length
n	High-Fidelity Enthalpy-Based Stanton Number Exponent
n'	Regression Rate Model Burn Exponent
r	Fuel Port Radius
x	Longitudinal Length Downstream of Injector
α	Optical Absorbtivity
β	Lee’s Blowing Coefficient
γ	Combustion Product Specific Heat Ratio
Δh	Flame Surface Enthalpy Change
ϵ	Optical Emissivity
μ	Dynamic Viscosity of Boundary Layer Product
τ	Skin Friction Coefficient Scale Factor

CHAPTER I

INTRODUCTION

Conventionally, satellite manufacturing has been based solely upon large-scale structures and prosperous corporations for commercial applications in satellite telecommunications, surveillance, and broadcasting. These satellites are launched through rideshare opportunities via launch service providers such as United Launch Alliance (ULA), Airbus, International Launch Services (ILS), and Space Exploration Technologies (SpaceX) [1]. However, with the increasing interest towards micro-gravity experiments, the demand of small satellites built by academic institutions, and the appeal of launching small satellite constellations, a cost-effective launch solution that can cater towards a smaller budget, is in need. Up to half of the total cost of small satellite missions is due to launch, and the additional uncertainty of pricing and scheduling can delay or even prevent many small satellite launch campaigns. This hinders the endeavors of aerospace aspiring countries, halting progress in science, technology, and defense.

“Small satellites are currently under-served when it comes to dedicated and timely launch opportunities, and addressing this issue is of particular relevance for the UK,” as stated in a report by Conor O’Sullivan, a business manager for a UK space organization – Satellite Applications Catapult. “The UK currently has world-leading capability in all parts of the satellite industry value chain, except launch. This limitation makes the UK vulnerable to launch price and schedule changes from international partners and suppliers and poses an increasing risk to achieving the UK space sector’s ambitious growth targets.” The concern towards dependency on existing launch service providers is not limited to the UK. Space-based access is becoming a global endeavor in the interest of Earth observation missions to help resource management, agriculture, and mapping. This includes multiple countries from Nigeria to Kazakhstan [2].

Multiple emerging private companies are responding to the need of dedicated small satellite payload launch vehicles, such as Aerojet Rocketdyne's Spaceborne Payload Assist Rocket (SPARK), Virgin Galactic's LauncherOne, and Rocket Lab's Electron small satellite launchers. This industry is a new and rapidly evolving aerospace sector, where system simplicity, rapid manufacturing, low cost, and characterized motor performance are of primary importance. Hybrid rocket motors provide a cheaper and less complex alternative to liquid propellant motors, while maintaining the capability to throttle and restart. In addition, HRMs produce specific impulse levels superior to solid rocket motors and bypass the hazards of manufacturing, handling, and shipping that are inherent to solid rocket fuels. As such, HRMs offer a competitive choice for upper stages or air-launch propulsion systems for small satellite missions that require precise orbital insertion.

Hybrid rocket motors not only serve as a viable solution for small satellite launchers, but also as add-on small satellite propulsion units for ΔV maneuvers and end-of-life deorbit strategies. The Low Earth Orbit (LEO) space debris environment is becoming a critical issue with the increasing demand of placing satellites in space. Roughly 2 million kilograms of uncontrolled debris has accumulated in LEO and the probability of collisions between spacecraft and debris will grow up to a rate of 5% per year if no action is taken. Many spacecraft are at risk from both large collisions and millimeter-sized particle impacts due to the high orbital speeds in LEO. A global collaboration, Inter-Agency Space Debris Coordination Committee (IADC), was formed as a response to regulate orbital debris and formed a set of guidelines known as the IADC Space Debris Mitigation Guidelines. Section 5.3.2 of this document states:

> Whenever possible spacecraft of orbital stages that are terminating their operational phases in orbits that pass through the LEO region, or have the potential to interfere with the LEO region, should be de-orbited or where appropriate maneuvered into an orbit with a reduced lifetime [3].

Thus, small spacecraft companies now face the additional requirement of deorbit capability. This presents a challenge to maintain a lite-weight, benign, and low-cost propulsion unit that will not pose a threat to the primary spacecraft payload. A hybrid rocket propulsion module offers a solution to this dilemma due to their relatively simplistic design, low power requirement, non-toxicity, inexpensive components, and control fidelity.

When compared to conventional liquid- and solid-propelled rocket systems, hybrid rockets – where the propellants typically consist of a benign liquid or gaseous oxidizer and an inert solid fuel – possess well-known operational safety and handling-advantages. A study by the U.S. Department of Transportation concluded that hybrid rocket motors can be safely stored and operated without a significant risk of explosion or detonation, and offer the potential to significantly reduce operating costs for commercial launch vehicles [4].

Although the technologies that support practical applications of hybrid rocket motors have been well known for at least three decades, HRMs have not seen widespread use primarily due to their inherently low fuel regression rates and poor volumetric efficiency when compared to solid-fuel motors of the same impulse class. The low regression rate forces HRMs to require large amounts of oxidizer to match the thrust levels of equivalently-sized solid rocket motors. The resulting high oxidizer mass flux levels introduce potential issues with combustion stability, chaotic and erosive fuel burning, and nozzle erosion. Fortunately, multiple techniques have been recently developed to help mitigate the issues associated with low fuel regression rates, including metalized fuel, liquefying propellants, swirl injection, and introduction of helical fuel port geometries [5] [6]. As a result, HRMs have been since seeing increasing success, revealing several advantages such as manufacturability, handling, and non-toxicity. This recent technology readiness level (TRL) enhancement has led to extensive HRM performance characterization campaigns, both by academia and industry, in order to accurately predict hybrid motor behavior. Especially now, with the emergence of the small satellite industry, HRMs are revisited as a viable means to accomplish small- to medium-size satellite missions.

1.1 Additive Manufacturing of Hybrid Rocket Propellants

Whitmore and Peterson [7] at Utah State University have recently investigated the use of additively-manufactured acrylonitrile butadiene styrene (ABS) thermoplastic as a hybrid rocket fuel material. The key outcome of this research was the demonstrated thermodynamic equivalence of ABS to the conventional hybrid rocket fuel hydroxyl-terminated polybutadiene (HTPB) when burned with nitrous oxide (N_2O). ABS achieved a specific impulse (I_{sp}) and a characteristic velocity (c^*) that are nearly identical to

HTPB. Furthermore, ABS and HTPB fuel regression mass flow rates for cylindrical fuel ports were found to be nearly identical.

The process used to print these fuel grains is known as fused deposition modeling (FDM), which is a 3D printing method for thermoplastics, where a plastic filament is unwound from a coil and supplies material to an extrusion nozzle that heats the material to a near-liquid amorphous state. Once the material is layered, radiative cooling forms a solid material layer. The design starts from a 3D computer-aided design (CAD) model that is constructed by the developing engineer or technician. Once the CAD file is complete, the model is downloaded to the machine's processor and sectioned into layers that are built up one level at a time. Layer shapes are controlled in three dimensions via computer numerically controlled (CNC) mechanisms.

The use of FDM manufacturing circumvents many of the developmental issues normally associated with hybrid rocket systems and offers the potential to revolutionize the manufacture of hybrid rocket fuel grains. FDM can support high production rates and offers the potential of improving hybrid fuel grain quality, consistency, and performance, while reducing development and production costs. These manufacturing advantages are not achievable using the conventional methods of solid propellant production.

ABS has several mechanical properties that make it very attractive as a hybrid rocket fuel – being an inexpensive thermoplastic material that is widely mass-produced for a variety of non-combustion applications, including household plumbing and structural materials. It is a non-crystalline material with an amorphous structure, which means that ABS does not possess a true melting point, but exists in a highly softened semi-fluid state before vaporizing. A typical glass transition temperature for ABS plastics is 105°C and this semi-fluid state exists over a wide range of temperatures. As such, ABS has become one of the most commonly-used materials in FDM printers [8].

Almost any conceivable shape can be printed using FDM. Multiple vendors using a well-developed commercial technology can produce identical pieces simultaneously. Because the components are built additively, designs are highly scalable. This has enabled the capability to print hybrid rocket fuel to any size desired, from a launch vehicle down to small satellite propulsion. Figure 1.1 shows some of the scales of hybrid rocket fuels that have been successfully fabricated using additive manufacturing.

Figure 1.1: Scalable Fuel Grains Possible through Additive Manufacturing

Along with the mechanical and structural advantages, certain 3D printed thermoplastics – ABS being one of them – are semi-electrically-conductive. When subjected to a high-voltage, low-current charge, electrostatic arcing along the surface pyrolyzes a small amount of material, which produces a rich hydrocarbon vapor. When an oxidizer is introduced, the electrical arcing seeds combustion and produces immediate and reliable ignition [9].

Due to the advantages in structural, as well as ignition capabilities, printed thermoplastic materials such as ABS have proved to be an excellent fuel source, outperforming other common small spacecraft propulsion fuels such as hydrazine [10]. Multiple test campaigns have been completed to prove the feasibility of ABS as a hybrid rocket fuel, and an interesting outcome has revealed itself: a natural burn behavior that shifts the oxidizer-to-fuel (O/F) ratio from an initial slightly fuel-lean proportion to a highly fuel-enriched burn proportion near the end of the burn. In combustion chemistry, a stoichiometric burn consumes all of oxidizer and fuel in a propellant mix. For a lean burn, the entire fuel component has been consumed and an unburned quantity of oxidizer remains. On the other hand, a rich burn consumes all the oxidizer with left-over fuel remaining [11]. Figure 1.2 illustrates this behavior for a lab-scale 38-mm motor with an additively-printed ABS fuel grain. The sequence of images displays the plume during an 8-second continuous burn. For this motor, the length was tuned to give an O/F slightly greater than the stoichiometric point (~ 2.0) for the initial part of the burn, with the O/F dropping to less than 0.5 by the end of the burn. The shift from lean to rich is clearly visible.

This result is in direct contrast to the normally-observed burn properties of hybrid rockets [12]. For most HRMs, O/F ratio changes over time due to the natural expansion of the fuel port diameter as the fuel regresses. Because the cross section area of the motor grows at a rate that is higher than the surface burn area according to the port diameter, the oxidizer mass flux drops with time and the fuel regression rate drops accordingly. Thus, the behavior exhibited by printed ABS is a clear anomaly. This study examines the hypothesis that radiative energy transfer in small-scale printed fuel motors is responsible for the observed lean-to-rich O/F shift. The magnitude of this radiation term was negligible for the motor scales and types of propellants that had been previously tested. To prove this hypothesis, a detailed enthalpy balance model was developed and tested using experimental fuel regression rate data obtained from a variety of motor scales using printed ABS fuel grains.

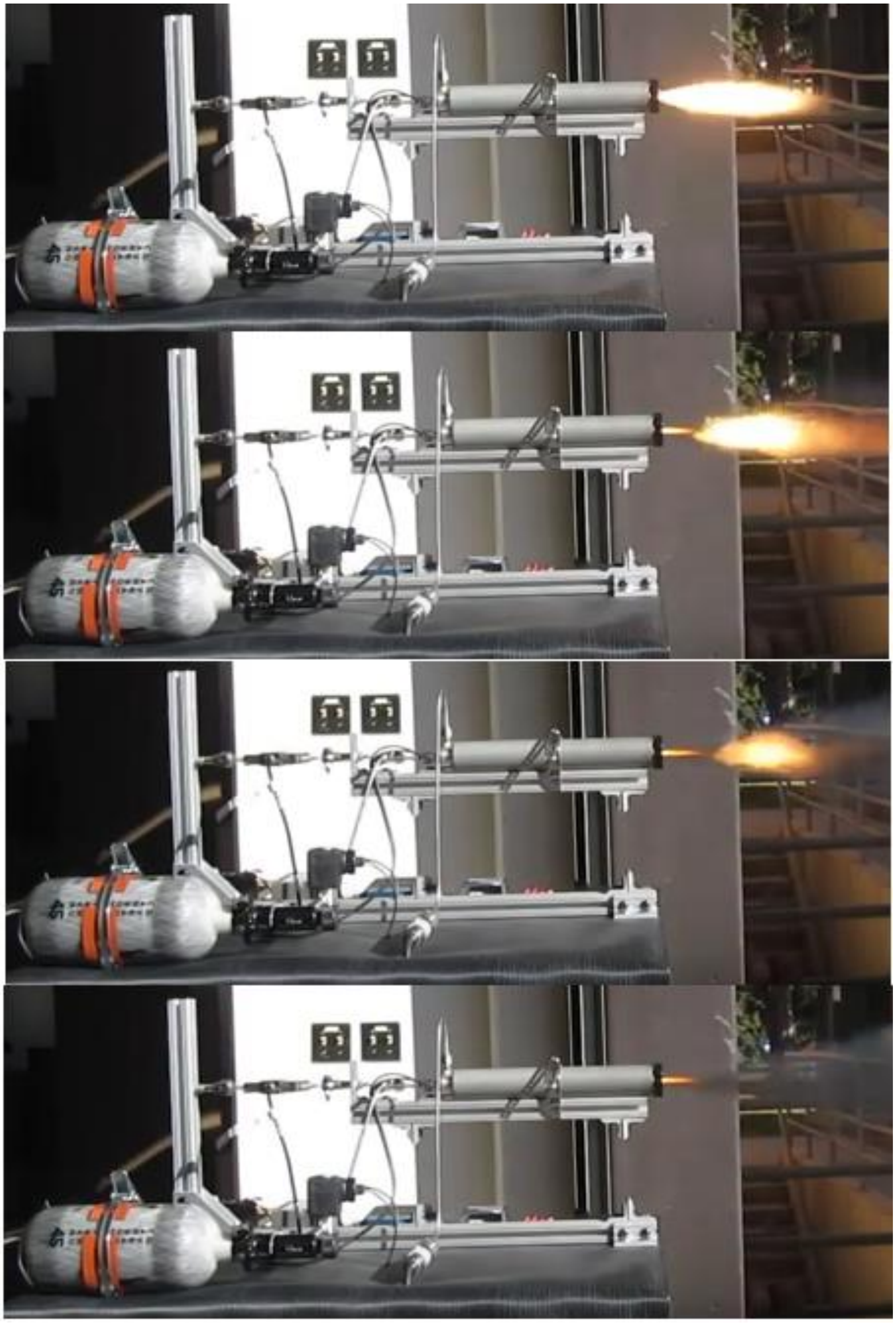

Figure 1.2: Image Sequence Showing Fuel-Rich Burn Behavior of a 38-mm Test Motor

CHAPTER II

AN OVERVIEW OF HYBRID ROCKET COMBUSTION BALLISTICS

Hybrid rocket motors generate combustion through processes that involve flow, similar to bi-propellant motors. The difference, however, is that bi-propellant motors have oxidizer and fuel mass flow rates that can be independently determined. Hybrid motors have fuel flow rates that are intrinsically linked to the oxidizer flow, preventing independent specification. As such, the ability to determine fuel regression rate is paramount, although very difficult due to its coupling with heat transfer, boundary layer effectiveness, chamber pressure, combustion volume, and oxidizer mass flow. This makes hybrid rocket performance analysis very empirically-based, lacking a comprehensive theory. As succinctly put by Zilliac and Karabeyoglu [13]:

> Hybrid rocket fuel average regression rate is one of the most important values to accurately determine the hybrid rocket design process and for rocket performance prediction. Yet there is no comprehensive theory that can be used to reliably predict this quantity. Additionally, regression rate data is difficult to measure. Measured data often contains a high degree of scatter, suffers from scale effects and is generally a closely-held secret by those performing the experiments and therefore is unavailable for many propellant combinations.

The pioneers of hybrid rocket combustion theory, Marxman and Gilbert [14], used modeling to determine that the efficiency of combustion is a function of diffusion effectiveness into the combustion layer, or flame sheet, between the axially-flowing oxidizer and the radially vaporizing fuel. This is depicted in Figure 2.1 [13],

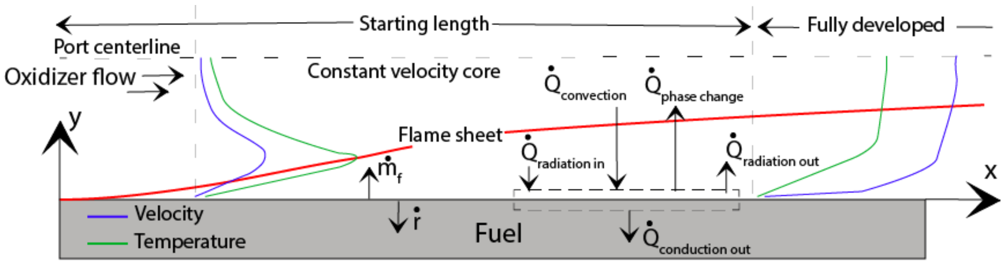

Figure 2.1: Hybrid Rocket Motor Combustion Concept

This concept provides a good description that includes convective and radiative energy transfer mechanisms. Conductive energy transfer throughout the fuel grain is minimal because most thermoplastics and waxes ablate at the surface exposed to the combustion flame before transferring energy further into the material. Marxman’s model also reveals why hybrid rocket motors have low fuel regression rates, which is due to the outflowing fuel into the flame sheet. The outflowing fuel essentially pushes the combustion layer further away from the fuel surface, causing combustion to be less effective and decreasing the efficiency of diffusion at the flame sheet (Figure 2.2). This phenomenon has been termed “wall blowing” and it is the main reason that HRMs have low fuel regression rates compared to solid rocket motors [15]. Multiple techniques have been implemented to help reduce this effect, but wall blowing is inherent to all hybrid rocket designs and cannot be avoided unless a completely different propulsion system is used.

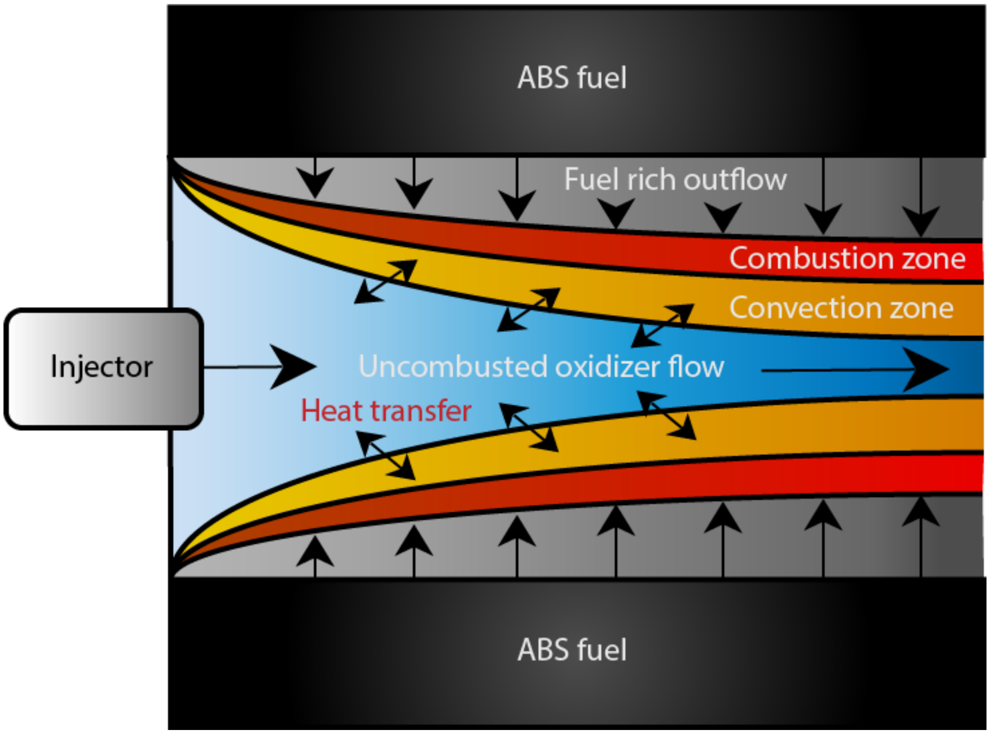

Figure 2.2: Radial “Wall Blowing” Concept

2.1 Effects of Hybrid Rocket Motor Oxidizer-to-Fuel Ratio on Combustion Properties

The O/F ratio, also known as the fuel mixture ratio, is a mass-based parameter that quantifies HRM performance. When characterizing combustion behavior, the stoichiometric O/F ratio is of interest because it provides the highest combustion temperature. However, when optimizing motor performance, an O/F ratio that operates slightly lower than the stoichiometric point is desired due to a balance between temperature and exhaust product molecular weight. A complete stoichiometric reaction will produce heavier molecules than a slightly fuel-rich O/F ratio, which allows for lighter fuel molecules, such as hydrogen, to remain unreacted; producing a higher specific impulse [16]. But there are two primary drawbacks in hybrid rocket motors that involve the O/F ratio – the first is that hybrid rocket O/F ratios shift; even during steady-state combustion, which further complicates the prediction of performance. Second, HRMs have very minimal fuel regression rates for a given amount of oxidizer flow, causing O/F ratios to increase far from optimal. These issues are inherent to the physics of hybrid rocket combustion, unfortunately. Combustion is governed by flow inside of a spatially-transient combustion chamber since the fuel itself determines the volume, which is burning away as the motor operates. As such, the combustion physics that describe hybrid motors is complicated, despite all of its practical benefits as a propulsion system. Most propellant combinations for HRMs have an O/F ratio tendency to become more oxidizer-rich throughout burning and have optimal O/F ratios that are very oxidizer-dominant, such as HTPB burned with N_2O, which has an optimal O/F ratio of about 6. In contrast, ABS and gaseous oxygen (GOX) display an O/F ratio tendency to become more fuel-rich throughout burning and have an optimal O/F ratio of about 2.

2.2 Motor Scaling Effects

Throughout all of the analysis accumulated for hybrid rockets, three distinct regimes of combustion characteristics have been identified as a function of mass flow per cross-sectional area (mass flux). These regimes lie within low, medium, and high mass flux levels. Table 2.1 summarizes these identified regions of operation [16].

The most recent hybrid rocket ballistics models are based on medium-level mass flux since most practical hybrid rocket applications operate within this region. But with the capability to additively manufacture fuels and the interest in benign small spacecraft propulsion systems, small-scale HRMs are being extensively investigated. Small-scale motors typically come with small oxidizer mass flow levels, which in turn produce small oxidizer mass flux levels. This calls for analysis within the low mass flux level regime, meaning that radiative energy transfer becomes a term that can no longer be neglected. Furthermore, during the course of operation of a small-scale motor, the port diameter widens as the fuel is burned away and the mass flux levels decrease further still due to the increase in cross-sectional area. The effect of radiative energy transfer amplifies as the combustion chamber becomes saturated with fuel particles and the oxidizer mass flux decreases, continuing until the solid fuel is depleted. As a result, the O/F ratio becomes very fuel-rich and increasingly so as a function of burn duration.

Table 2.1: Hybrid Rocket Combustion Characteristics as a Function of Mass Flux

Mass Flux Level	Low	Medium	High
Description	Radiative heat transfer dominates due to optical transmissivity of propellant particles	Convective diffusion dominates as well as fully turbulent heat and mass transfer	Gas-phase kinetics on chemical reactions become more apparent

2.3 Exponential Curve Fit Regression Rate Model

Solid rocket motor fuel regression is a function of propellant combination and combustion chamber pressure, as shown in the following equation:

$$\dot{r} = aP_0^{n'} \tag{2.1}$$

where P_0 is the chamber pressure; and, a and n' are empirically derived constants based on propellant formulation. Equation 2.1 is known as Saint Robert's Law [15], which was originally used to understand the behavior of gunpowder. A similar exponential curve fit regression rate model has been implemented for hybrid rocket motors – the difference being that the driving factor is oxidizer mass flux (G_{ox}) instead of chamber pressure:

$$\dot{r} = aG_{ox}^{n'} \tag{2.2}$$

The empirical values of a and n' have been determined for multiple propellants and reveal regression rate values approximately between 0.05-0.3 cm/s, aside from paraffin fuel, which exhibits amplified fuel regression rates in comparison. As a function of oxidizer mass flux (which decreases as a function of burn time), the behavior of fuel regression rate can be analyzed graphically. Figure 2.3 displays a side-by-side comparison of fuel regression rates from other HRM studies [12] [21] and HRM studies conducted at Utah State University (USU) using ABS/GOX propellant combinations. The encompassing study of all ABS/GOX HRMs conducted at USU involved many motor configurations including motor diameters of 98-, 75-, 54-, 38-, and 24-mm sizes. The 38-mm motor configuration was additionally tested for two different lengths, where S38mm represents the shorter motor and L38mm represents the longer motor.

Figure 2.3 shows fuel regression rate values that were curve fitted through the exponential model of Eq. 2.2. The values of regression rate are similar across all studies, as well as the behavior, which shows that fuel regression rates decrease with oxidizer mass flux. The primary difference lies within the values of the burn exponent, n'. The exponential curve fit model burn exponents regarding ABS/GOX propellants tested at

USU have values that are less than 0.5, whereas the other HRM studies have values that are greater than or equal to 0.5. Upon analyzing the O/F ratio between the two-test series, the contradictory fuel-rich behavior is revealed.

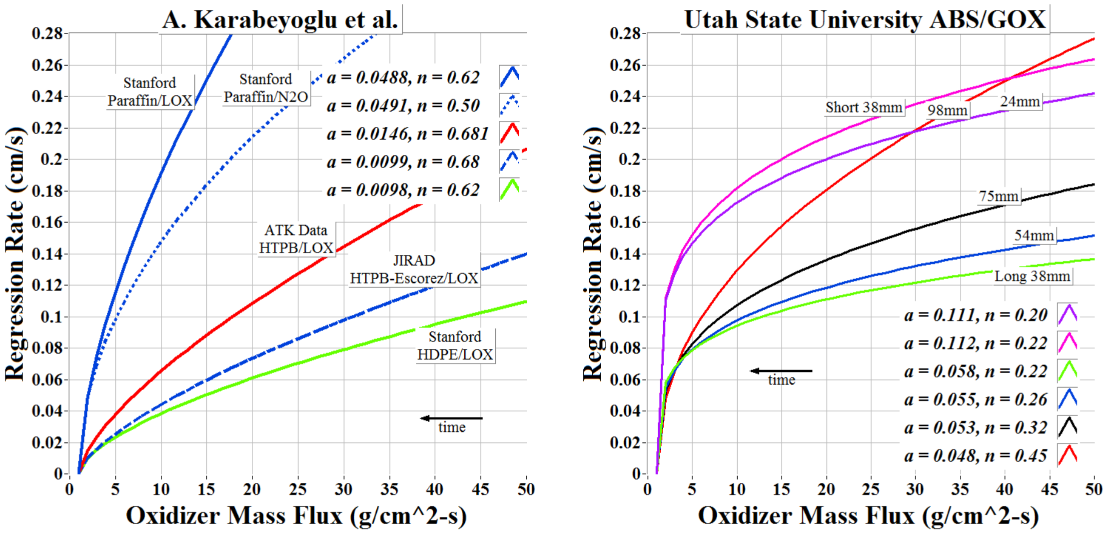

Figure 2.3: Side-by-Side Comparison of Fuel Regression Rates as a Function of Oxidizer Mass Flux for Multiple HRM Propellant Combinations [12] [21] and ABS/GOX Propellant Combination

In order to extrapolate the O/F ratio from the empirical scale factors and burn exponents according to the HRM regression rate data obtained through A. Karabeyoglu, et al. [12] [21], an O/F ratio manipulation is derived. The derivation begins by considering the ratio of O/F ratio to initial O/F ratio (expressed as $(O/F)_0$),

$$\frac{O/F}{(O/F)_0} = \frac{\dot{m}_{ox}}{\dot{m}_f}\left(\frac{\dot{m}_{f_0}}{\dot{m}_{ox}}\right) = \frac{\dot{m}_{f_0}}{\dot{m}_f} \tag{2.3}$$

After expanding the fuel mass flow terms and reducing,

$$\frac{O/F}{(O/F)_0} = \frac{\rho_f \dot{r}_0 A_{b_0}}{\rho_f \dot{r} A_b} = \frac{\dot{r}_0 D_0}{\dot{r} D} = \frac{a G_{ox_0}^{n'} D_0}{a G_{ox}^{n'} D} = \left(\frac{D}{D_0}\right)^{2n'-1} \tag{2.4}$$

Leaving Eq. 2.4 aside for a moment, the initial O/F ratio can be expressed as,

$$(O/F)_0 = \frac{\dot{m}_{ox}}{\dot{m}_{f_0}} = \frac{\dot{m}_{ox}}{\rho_f A_{b_0} \dot{r}_0} = \frac{\dot{m}_{ox}}{\rho_f \pi D_0 L \left(a {G_{ox}}_0^{\,n'}\right)} = \frac{\dot{m}_{ox}^{1-n'}}{\rho_f \pi^{1-n'} 4^{n'} L a} D_0^{2n'-1} \tag{2.5}$$

After including Eq. 2.5 in Eq. 2.4, the O/F ratio is expressed as a function of the port diameter ratio and initial-port-diameter-to-length ratio,

$$O/F = \frac{{G_{ox}}_0^{\,1-n'}}{4 a \rho_f} \left(\frac{D_0}{L}\right) \left(\frac{D}{D_0}\right)^{2n'-1} \tag{2.6}$$

Using an initial oxidizer mass flux and initial-port-diameter-to-length ratio of 20 g/cm^2-s and 0.2, respectively, and using fuel material densities of 0.975, 0.93, 0.90, and 0.97 g/cm^3 for ABS, paraffin, HTPB, and HDPE, respectively, a side-by-side comparison of O/F ratio as a function of fuel port diameter ratio (ratio of instantaneous diameter to initial diameter) between multiple HRM propellant combinations and ABS/GOX propellant combination is shown in Fig. 2.4.

Figure 2.4 represents the crux of this thesis – displaying that the O/F ratio shift exhibited in small-scale ABS/GOX hybrid rocket motors is in direct contrast with other studied HRMs. When analyzing Eq. 2.6 using constant arbitrary values for a burn exponent greater than, equal to, and less than 0.5, Fig. 2.5 summarizes the effect of the empirical burn exponent on the O/F ratio shift.

Figure 2.5 summarizes the contrast between the two-test series in Fig. 2.4 – burn exponents greater than 0.5 exhibit fuel-lean O/F ratio shifts whereas burn exponents less than 0.5 exhibit fuel-rich O/F ratio shifts. As the burn exponent becomes greater than 0.5, so does the amplitude of the fuel-lean O/F shift, whereas when the burn exponent recedes further from 0.5, the amplitude of the fuel-rich O/F shift increases. This has been observed qualitatively in Figure 1.2 and shown quantitatively via the exponential curve fit regression rate model.

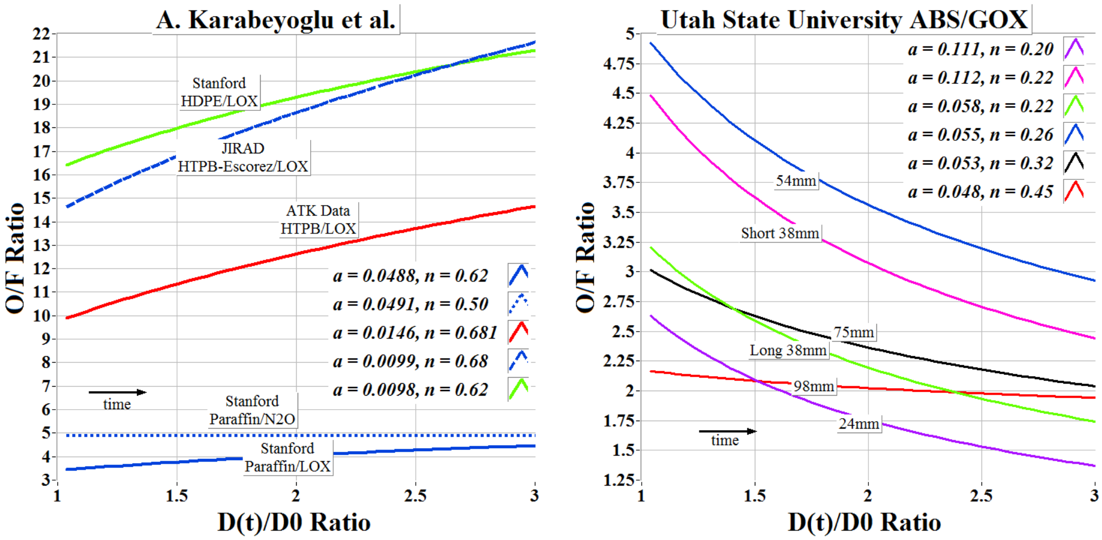

Figure 2.4: Side-by-Side Comparison of O/F Ratio as a Port Diameter Ratio for Multiple HRM Propellant Combinations and ABS/GOX Propellant Combination

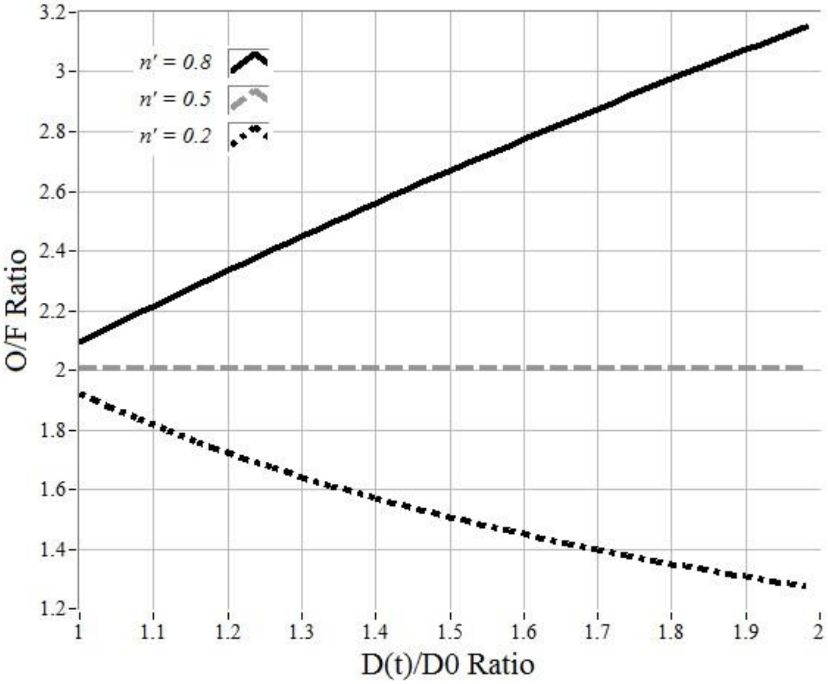

Figure 2.5: O/F Ratio Trend with Varying Burn Exponents and Arbitrary Motor Parameters

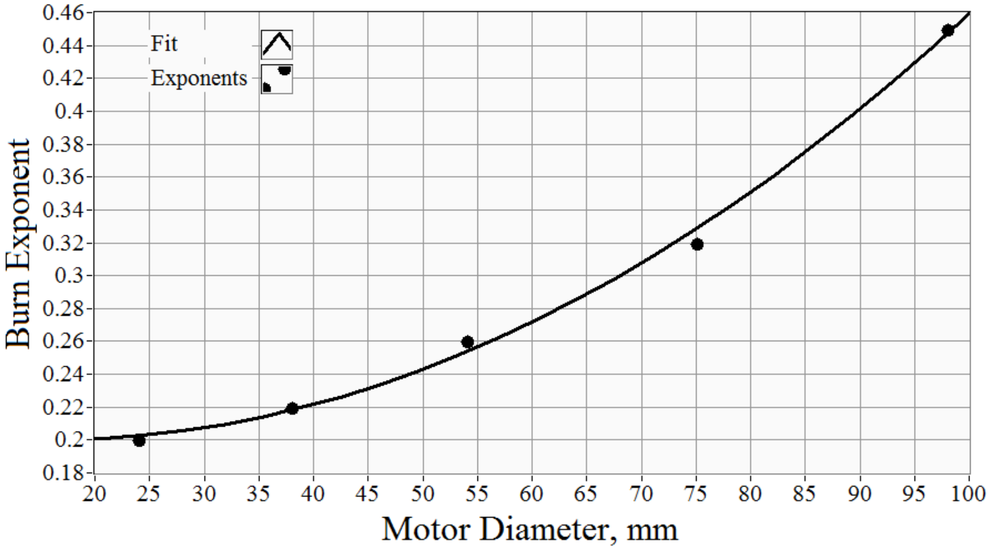

Figure 2.6: Burn Exponent as a Function of Motor Diameter for HRMs Using ABS/GOX

Equation 2.2 is an excellent model for predicting HRM fuel regression rates but lacks a comprehensive theory as to why or how the empirical values are determined, besides fitting the experimental data. Even if a and n' are empirically determined, they are susceptible to becoming inaccurate with small changes in multiple parameters such as motor length, nozzle geometry, and burn time. As such, Eq. 2.2 involves a high degree of tailoring – not only to specific propellant combinations, but also to particular HRM specifications and flight conditions. Furthermore, Eq. 2.2 is a port-length-averaged fuel regression rate and does not account for local port diameter as a function of axial distance, which can vary up to 10%. Often termed as fuel port 'bowing', this effect is readily seen in the axial cross-section of HRM fuels depicted in Fig, 2.7.

Figure 2.7: Fuel Port Bowing Effect in Samples of Burned Fuel Cells

Regardless of the complications, Eq. 2.2 is still widely used and serves well when a timely and cost-effective HRM propulsion unit is in need without the finer details that are usually only of concern to academia. However, a higher-fidelity model is required because the empirical burn exponents cannot be determined effectively with multiple tests alone. It has been shown that the O/F ratio trend is ultimately governed by the burn exponent but does not explain the reasoning behind its value, since it is simply an empirical curve fit with no theoretical foundation.

The observation shown in Fig. 2.6 partially explains the results presented by Figs. 2.4 and 2.5. Clearly, there are more effects at work than the simple enthalpy balance explained by classical Marxman theory. The following section will extend the original Marxman theory to account for the effects of radiative energy transfer. Dimensional analysis will demonstrate that these radiative effects become more significant as the motor diameter decreases, and eventually offsets the drop in convection with decreasing oxidizer, as predicted by Marxman. The trend towards fuel-richer burns for small fuel grains is thereby justified.

2.4 Enthalpy Balance Regression Rate Model with Convection

The higher-fidelity HRM fuel regression model begins with an energy balance – the basic idea being that the energy causing the solid fuel to ablate must be equal to the energy transfer mechanisms occurring within the combustion flame sheet. Most HRM propellant combinations and geometries that have been studied extensively are dominated by oxidizer flow, such as hydroxyl-terminated polybutadiene (HTPB) and nitrous oxide (N_2O), which will typically see O/F ratios of 6. This has allowed convection-only energy transfer to be a reasonable assumption when implementing the energy balance fuel regression model. In addition, hybrid rocket fuels tend to vaporize at the surface exposed to heat and sometimes form char-melt layers, which serve as additional insulation to the remaining fuel. This makes heat transfer via conduction into the fuel grain almost non-existent, and can be considered negligible. The steady-state energy balance is written in the form of energy flux density, having units of power per cross-sectional area:

$$\dot{Q}_{fuel\,ablation} = \dot{Q}_{convection} \tag{2.6}$$

Using the dimensionless Stanton number, which is the ratio of the energy transferred and the thermal capacity of the flame sheet, an expression for the energy flux density can be formed. The fuel regression rate reveals itself upon expanding the energy flux density due to fuel ablation, as follows:

$$\dot{r}\rho_f h_v = S_t \rho_c u_c \Delta h \tag{2.7}$$

where $\dot{r}$ is the axial fuel regression rate; ρ_f is the fuel density; h_v is the fuel's specific heat of vaporization; S_t is the Stanton number; ρ_c is the density of the combustion product; u_c is the velocity of the combustion product; and, Δh is the change in enthalpy between the combustion zone and the fuel surface. The product of the combustion product density and velocity results in the accumulated total mass flux, which is essentially the combination of the oxidizer mass flux with the fuel mass flux. But this product is assumed to be the oxidizer mass flux alone, which simplifies the derivation. After implementing the assumption of oxidizer-dominant flow and solving for the regression rate, Eq. 2.7 becomes

$$\dot{r} = \frac{S_t G_{ox} \Delta h}{\rho_f h_v} \tag{2.8}$$

where G_{ox} is the oxidizer mass flux and the enthalpy difference, Δh, can be expanded into identifiable parameters:

$$\Delta h = c_{p_c}\left(T_0 - T_f\right) \tag{2.9}$$

where c_{p_c} is the isobaric specific heat of the combustion product; T_0 is the combustion flame temperature; and, T_f is the temperature of the fuel grain surface. For brevity, Δh will remain in its unexpanded form throughout the remainder of this report. Equation 2.9 is used for reference purposes.

The energy-balance model thus far contains many readily-available parameters that can be accurately deemed as constant, such as oxidizer mass flow (when not throttling), fuel density, latent heat of vaporization, and fuel surface temperature. Additionally, during steady-state conditions, the majority of thermodynamic properties of the combustion flame can also be considered constant. But the main complication presents itself within the Stanton number, which introduces myriad empirical correlations, assumptions, and special conditions. This study implements the techniques used by Whitmore, et al., without further investigation into thermodynamic correlations [17]. The Stanton number can be expanded using the Chilton-Colburn analogy:

$$S_t = \frac{1}{2} C_f P_r^{-\frac{2}{3}} \tag{2.10}$$

where C_f is the skin friction coefficient and P_r is the Prandtl number. Due to the wall-blowing effect depicted in Fig. 2.2, the boundary layer mixing between oxidizer and fuel requires a correction to the skin friction coefficient. This is accomplished through Lee's model that accounts for radially emanating flow fields:

$$C_{f_B} = \frac{1.27C_f}{\beta^{0.77}} \tag{2.11}$$

where C_{f_B} is the skin friction coefficient correction in the presence of radial wall blowing; and, β is Lee's blowing coefficient, which is a ratio between the surface emanating mass flux and the oxidizer mass flux [18]. Boardman [5] simplified Lee's blowing coefficient further by characterizing it as the ratio between the combustion enthalpy difference and the fuel latent heat of vaporization:

$$\beta = \frac{\Delta h}{h_v} \tag{2.12}$$

Now it is possible to define the Stanton number in terms of readily-available parameters, resulting in the expansion of Eq. 2.8 into:

$$\dot{r} = \frac{0.635C_f G_{ox}\Delta h}{\rho_f P_r^{\frac{2}{3}}\beta^{0.77}h_v} \tag{2.13}$$

The final term that requires further expansion is the skin friction coefficient, C_f. Whitmore, et al., modeled the skin friction coefficient as a product between the skin friction coefficient scale factor and local Reynolds number [19]:

$$C_{f_x} = \tau Re_x^{n-1} = \tau\left(\frac{\rho_c u_c x}{\mu}\right)^{n-1} = \tau G_{ox}^{n-1}\left(\frac{\mu}{x}\right)^{1-n} \tag{2.14}$$

In order to obtain a port-length-averaged value, the local skin friction coefficient is integrated through the port length and divided by the total port length

$$C_f = \frac{1}{L}\int_0^L C_{f_x} dx = \frac{\tau G_{ox}^{n-1}\mu^{1-n}}{L}\int_0^L \left(\frac{1}{x}\right)^{1-n} dx = \frac{\tau}{n} G_{ox}^{n-1}\left(\frac{\mu}{L}\right)^{1-n} \tag{2.15}$$

By replacing C_f in Eq. 2.13 with the expression in Eq. 2.15, the final regression rate formula becomes:

$$\dot{r} = \frac{0.635\tau G_{ox}^{\mathrm{n}}}{n\rho_f P_r^{\frac{2}{3}}\beta^{0.77}}\left(\frac{\Delta h}{h_v}\right)\left(\frac{\mu}{L}\right)^{1-n} \tag{2.16}$$

It should be noted that the exponent, n, displayed in Eq. 2.16 is not the same as the burn exponent shown in Eq. 2.2. A certain level of ambiguity exists with regard to determining the skin friction coefficient scale factor, τ, and the exponent factor, n. Normally, the Blasius formula for turbulent wall shear stress is used for τ, which has a value of 0.0592 [20]. The value of the exponent, n, has been determined to have a value of 0.8, which has remained unchanged since Marxman's original derivation [14]. For ABS/GOX propellant combinations, the regression rate described by Eq. 2.16 under-predicts the combustion-chamber pressure collected from experimental data, demonstrating that the classical Marxman model is not necessarily incorrect, but incomplete for small-scale ABS/GOX propellant combinations.

2.5 Proposed Enhancements to the Marxman Fuel Regression Rate Model

The initial inclination towards investigating radiative effects comes from the summary in Table 2.1, which suggests that radiative energy transfer dominates at low mass flux levels. Disregarding the mass flux due to fuel mass flow, the oxidizer mass flux carried out within the experimental trials of this report are within the range of 2-20 g/cm^2-s, whereas the oxidizer mass flux ranges of other studies vary between 10-70 g/cm^2-s. However, mass flux ranges can reach the lower regions despite having high oxidizer mass flow because of larger port diameters, which implies larger port cross-sectional area. Thus, the underlying factor is the oxidizer mass flow level instead of the oxidizer mass flux level, which is between 6-8 g/s within the experimental trials of this study, as opposed 500-1000 g/s – the oxidizer mass flow levels for most previous HRM applications [21]. The very low oxidizer mass flow levels regarding the ABS/GOX hybrid rocket motors conducted at Utah State University is due to two reasons: the first being the low chamber pressure levels desired for small-scale thrusters, and second, the propellant combination used. Acrylonitrile butadiene styrene has combustion properties that offer stoichiometric combustion at O/F ratios of 2, and using GOX as an oxidizer requires the minimal oxidizer mass to achieve desired O/F ratios. As a result, trace amounts of oxidizer mass flow are required to achieve the desired performance of small-scale HRM thrusters. Low oxidizer mass flow levels initiate fuel-rich O/F behavior, but still exhibit greater fuel regression rate values because radiative effects dominate at these small-scale geometries as well as small mass flow levels. A concept of the physics involved depicted in Fig. 2.8 illustrate the low oxidizer mass flow, fuel-saturated, combustion chamber.

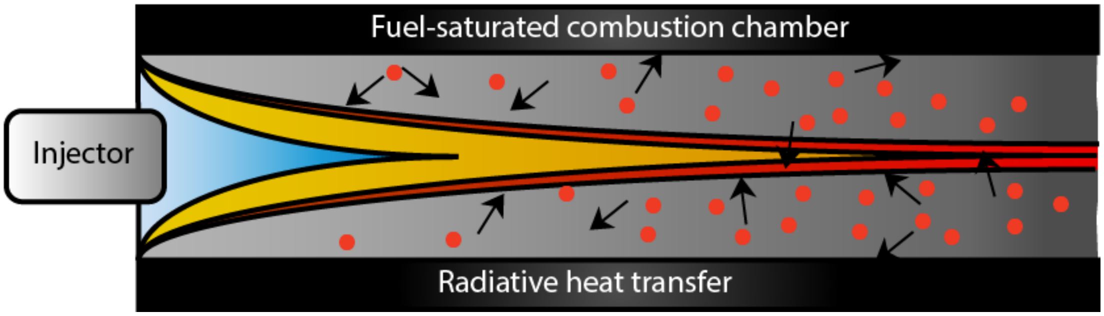

Figure 2.8: HRM Combustion Physics Concept in Small-Scale, Low Mass Flux Motors

Thus, despite the convention that more oxidizer mass flow initiates more aggressive fuel regression rates, a contradictory behavior is observed when the oxidizer mass flow and motor scale become small enough to operate within a different region of HRM burn characteristics – resulting in fuel regression rates that are comparable, if not higher, to typical fuel regression rates seen in the medium mass-flux regime.

2.6 Enthalpy Balance Regression Rate Model with Convection and Radiation

The radiation-adjusted regression rate model begins just as in section 2.4 – through an energy balance. The only difference is that the energy flux density due to radiative energy transfer is included:

$$\dot{Q}_{fuel\ ablation} = \dot{Q}_{convection} + \dot{Q}_{radiation} \tag{2.17}$$

Expanding each term within Eq. 2.17,

$$\dot{r}\rho_f h_v = S_t \rho_c u_c \Delta h + \sigma\left(\epsilon T_0^4 - \alpha T_f^4\right) \tag{2.18}$$

where σ is the Stefan-Boltzmann constant; ϵ is the optical emissivity of the combustion flame; T_0 is the temperature of the combustion flame; α is the optical absorptivity of the fuel grain; and, T_f is the surface temperature of the fuel grain. After implementing the

Stanton number and skin friction coefficient approximations that were carried out in section 2.4 and then solving for the regression rate, a result that is very similar to Eq. 2.16 is achieved:

$$\dot{r} = \frac{0.635\tau G_{ox}^{n}}{n\rho_f P_r^{\frac{2}{3}}\beta^{0.77}}\left(\frac{\Delta h}{h_v}\right)\left(\frac{\mu}{L}\right)^{1-n} + \frac{\sigma\left(\epsilon T_0^4 - \alpha T_f^4\right)}{\rho_f h_v} \tag{2.19}$$

Regardless of the addition of a new term in the energy balance equation, the radiation energy flux density term remains unaltered and the derivation of the convection energy flux density term does not involve any new technique. This means that Marxman's original derivation for the energy-balance-derived regression rate still holds true: τ is 0.0592 and n is 0.8. The only difference is the addition of a new radiation term, which becomes more prevalent depending on the HRM burn regime. Equation 2.19 can be further expressed as the addition of two terms that represent the regression rate due to convective energy transfer and radiative energy transfer,

$$\dot{r} = \dot{r}_{convection} + \dot{r}_{radiation} \tag{2.20}$$

Thus, the augmented Marxman model that accounts for radiation is simply an addition to the original model. It is evident that for larger oxidizer mass flux levels, the convective term dominates due to larger values of G_{ox}. For smaller oxidizer mass flux levels, the radiative term dominates where the key factor lies within the emissivity, ϵ, which depends on propellant combination, port diameter, motor length, and O/F ratio. Additionally, for burn durations longer than 4 s, the emissivity shifts. This is likely an artifact of accumulated fuel within the combustion chamber as a function of burn time with the addition of an increasing port diameter.

There is one correction factor to the convective term, however, when using the model in Eq. 2.20. This is correcting for wall blowing within a combustion chamber that has fuel mass flow which cannot be readily neglected. The correction method involves iterating Lee's blowing coefficient, β, to account for radiative-dominant wall blowing. In order to develop an iterative method for Lee's blowing coefficient, Boardman's approximation shown in Eq. 2.12 is used as the initial iteration. Further iterations are obtained from solving for the enthalpy ratio in Eq. 2.8:

$$\frac{\Delta h}{h_v} = \frac{\dot{r}\rho_f}{S_t G_{ox}} \tag{2.21}$$

Implementing Boardman's approximation and using the Chilton-Colburn analogy for the Stanton number:

$$\beta = \frac{2\dot{r}\rho_f P_r^{\frac{2}{3}}}{C_{f_x} G_{ox}} = \frac{2\dot{r}\rho_f P_r^{\frac{2}{3}}}{\tau G_{ox}^n \left(\frac{\mu}{x}\right)^{1-n}} \tag{2.22}$$

After integrating with respect to motor axial length and dividing by the total motor length:

$$\beta = \frac{2\dot{r}\rho_f P_r^{\frac{2}{3}}}{(2-n)\tau G_{ox}^n \left(\frac{\mu}{L}\right)^{1-n}} \tag{2.23}$$

In order to account for total mass flux, G_{ox} is replaced with the addition of oxidizer and fuel mass flux. Thus, the algorithm functions in the following order:

$$\beta^{(j=0)} = \frac{\Delta h}{h_v} \tag{2.24}$$

$$\dot{r}^{(j)} = \frac{0.635\tau G_{ox}^{n}}{n\rho_f P_r^{\frac{2}{3}}}\left(\frac{\Delta h}{h_v}\right)\left(\frac{\mu}{L}\right)^{1-n}\left(\frac{1}{\beta^{0.77}}\right)^{(j-1)} + \frac{\sigma\left(\epsilon T_0^4 - \alpha T_f^4\right)}{\rho_f h_v} \tag{2.25}$$

$$G_f = \dot{r}^{(j)}\rho_f \tag{2.26}$$

$$G = G_f + G_{ox} \tag{2.27}$$

$$\beta^{(j)} = \frac{2\dot{r}^{(j)}\rho_f P_r^{\frac{2}{3}}}{(2-n)\tau G^{n}\left(\frac{\mu}{L}\right)^{1-n}} \tag{2.28}$$

$$\dot{r}^{(j+1)} = \frac{0.635\tau G_{ox}^{n}}{n\rho_f P_r^{\frac{2}{3}}}\left(\frac{\Delta h}{h_v}\right)\left(\frac{\mu}{L}\right)^{1-n}\left(\frac{1}{\beta^{0.77}}\right)^{(j)} + \frac{\sigma\left(\epsilon T_0^4 - \alpha T_f^4\right)}{\rho_f h_v} \tag{2.29}$$

where j is the iteration count, G_f is the fuel oxidizer mass flux, and G is the total mass flux. Equations 2.24-2.29 conclude the proposed fuel regression rate model. It noted that this model is an addition to the original Marxman enthalpy balance model, where the Marxman exponent of n remains at a value of 0.8 – demonstrating that the classical model describes the flow properties and fluid mechanics within HRM combustion accurately, even for small-scale ABS/GOX HRMs. The classical model was incomplete with regard to the small-scale motors and required the addition of a radiative energy transfer term to fully capture this new regime of HRM performance.

2.7 Algorithm Programming Details

The algorithm was programmed in Matlab software and all of the thermodynamic properties for ABS/GOX combustion were obtained through the NASA Chemical Equilibrium with Applications (CEA) computer program. The results of a previous study conducted at Utah State University revealed the latent heat of vaporization of ABS to be 3 MJ/kg [9].

An initial O/F ratio estimate of 2 was implemented to begin numerical integration via a 4th-order Runge Kutta method, where the time-step was set at a constant $\Delta t = 1e^{-4}$ seconds. The integration involved a state array consisting of oxidizer mass flow, fuel mass flow, fuel regression rate, and the change of chamber pressure with respect to time. The equations describing these states are the compressible fluid injector equation, the product of fuel density and fuel regression rate, the regression rate equations established in this report, and an ordinary differential equation for transient chamber pressure, respectively. After each iteration, a new O/F ratio is backed out as the ratio between oxidizer mass flow and fuel mass flow, resulting in a new set of combustion thermodynamic properties to be determined via tabulated values acquired through CEA. This process was continued until the burn duration is complete.

Algorithm instabilities occur when the O/F ratio becomes unstable, which is almost always due to a poorly-predicted fuel regression rate (an additional reason why fuel regression rate analysis is paramount). This causes the fuel mass flow rate to be either too small or large, resulting in O/F ratio instability. Thus, algorithm success is not only determined by its ability to simulate experimental data, but also by its ability to remain stable. As a final note, 3-15 iterations of *j* seem to suffice for accurate correction regarding Lee's blowing coefficient within Eqs. 2.24-2.29. Figure 2.9 summarizes the algorithm in the form of a flow chart.

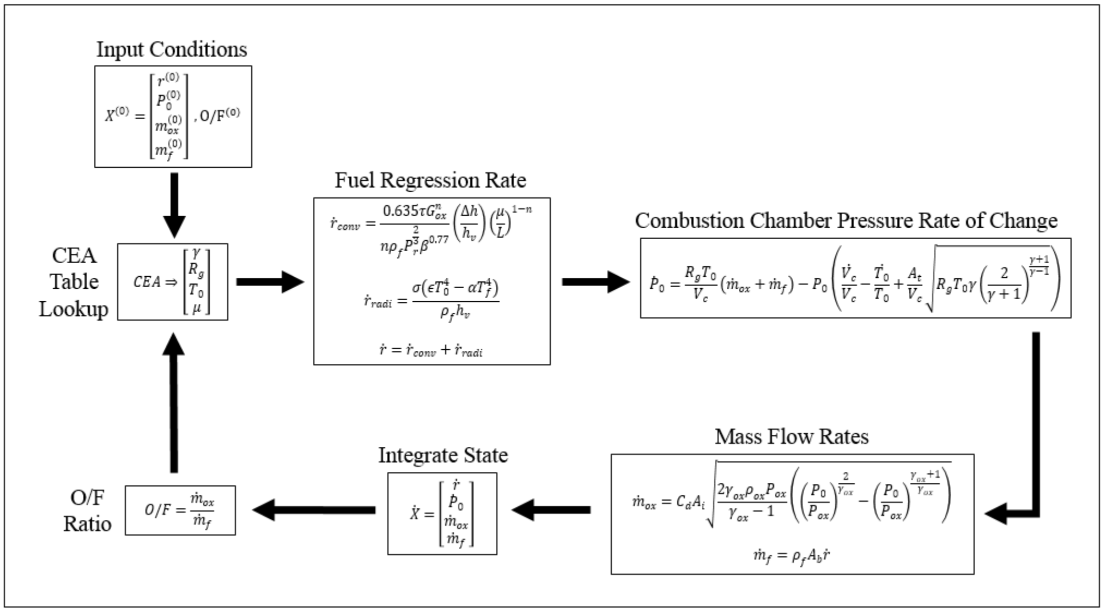

Figure 2.9: Algorithm Flow Chart Diagram

CHAPTER III

EXPERIMENTAL TEST EQUIPMENT SUMMARY

In order to investigate the observed fuel-rich O/F shift phenomenon of printed ABS fuel, an experimental campaign was performed using ABS/GOX propellants for a suite of test motors whose sizes varied from medium- (900 N) to small-scale (5 N). Commercially available solid rocket motor cases with 98-, 75-, 54-, 38-, and 24-mm external diameters were adapted as hybrid rocket chambers by replacing the motor separation charges with injector caps that were built in-house at Utah State University. The fuel grains were printed with interlocking sections using a Stratasys Dimension fused deposition modeling (FDM) printer. Figure 3.1 shows the general layout for these motors, which consists of the hybrid motor case, helical fuel grain interlocks, injector cap with ignition electrodes, and post-combustion chamber with a graphite nozzle insert.

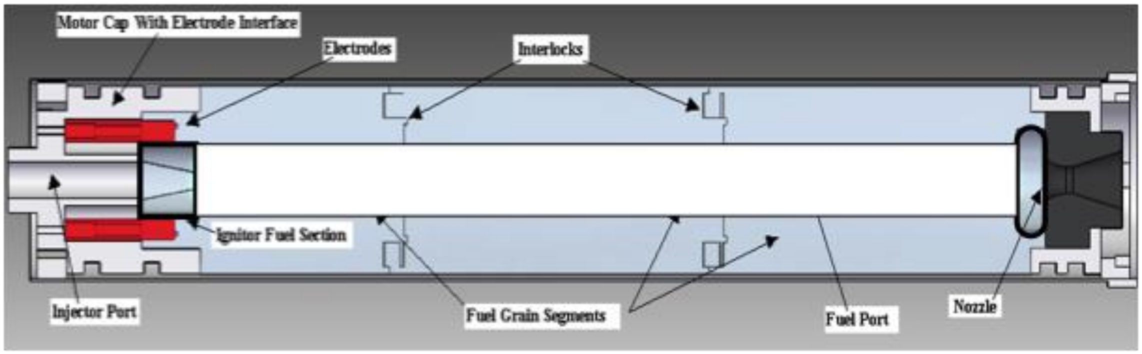

Figure 3.1: Schematic of Hybrid Motor Design with Snap-Together Fuel Grain Segments

The hybrid motor system is based on previous designs tested at Utah State University, where the printed fuel grain features “snap-together” interlocks that allow the grain segments to be manufactured separately and then assembled for combustion. Only the 38- and 24-mm motors were printed as a single piece due to their smaller size. The system is ignited using the patent-pending arc-ignition technology developed at Utah State University [7]. Table 3.1 gives a summary of the baseline motor layout geometry and performance parameters. The print density of all fuel grains was approximately 0.975 g/cm^3.

Table 3.1: ABS/GOX Hybrid Motor Test Geometry Summary

Motor No.	Case Diameter, mm	Fuel Grain Length, cm	Initial Port Diameter, cm	Chamber Pressure, kPa	Nominal Thrust Range, N	Nominal Oxidizer Massflow Rate, g/s	No. of Additional Tests During Thesis Duration
1	98	58.61	2.48	2900	800-900	225	-
2	75	35.98	2.03	1350	250-280	40	-
3	54	16.825	0.763	1650	25-30	5.5	-
4	38	18.415	0.635	650	7-15	3	23
5	38	6.812	0.635	830	7-18	2	8
6	24	7.645	0.33	1380	4-5	1.3	2

The 98-, 75-, and 54-mm motors were tested previously through other research endeavors conducted at Utah State University [5] [7] [9] [11] [17]. The study presented herein focused on testing the smaller-scale motors since these readily displayed the progressive plume “sootiness”, but the accumulation of these data with the previously-acquired data provided a vast motor geometry spread to test the ballistics model. Figure 3.2 displays the motor layout for the small-scale motors, including the short and long 38-mm and 24-mm diameter configurations with the corresponding aliases of Short MicroJoe (SMJ), Long MicroJoe (LMJ), and NanoJoe (NJ), respectively.

The test stand plumbing system involved a gaseous oxygen supply tank, pressure-reducing regulator, solenoid valve, and 5/16” outer diameter stainless steel tubing. All plumbing components were cleaned via ultrasonic bathing and fitted with GOX-compatible seals such as Viton and polyurethane. Omegadyne amplified sensors were used, including pressure transducers and a load cell for pressure and thrust measurements, respectively; type-K thermocouples for temperature measurements; and a custom-built Venturi flow meter for oxidizer mass flow rate. All data acquisition was carried out through National Instruments hardware and Labview software. Figure 4.2 shows a piping and instrumentation diagram for the test system and Fig. 4.3 outlines the components of the test stand at USU.

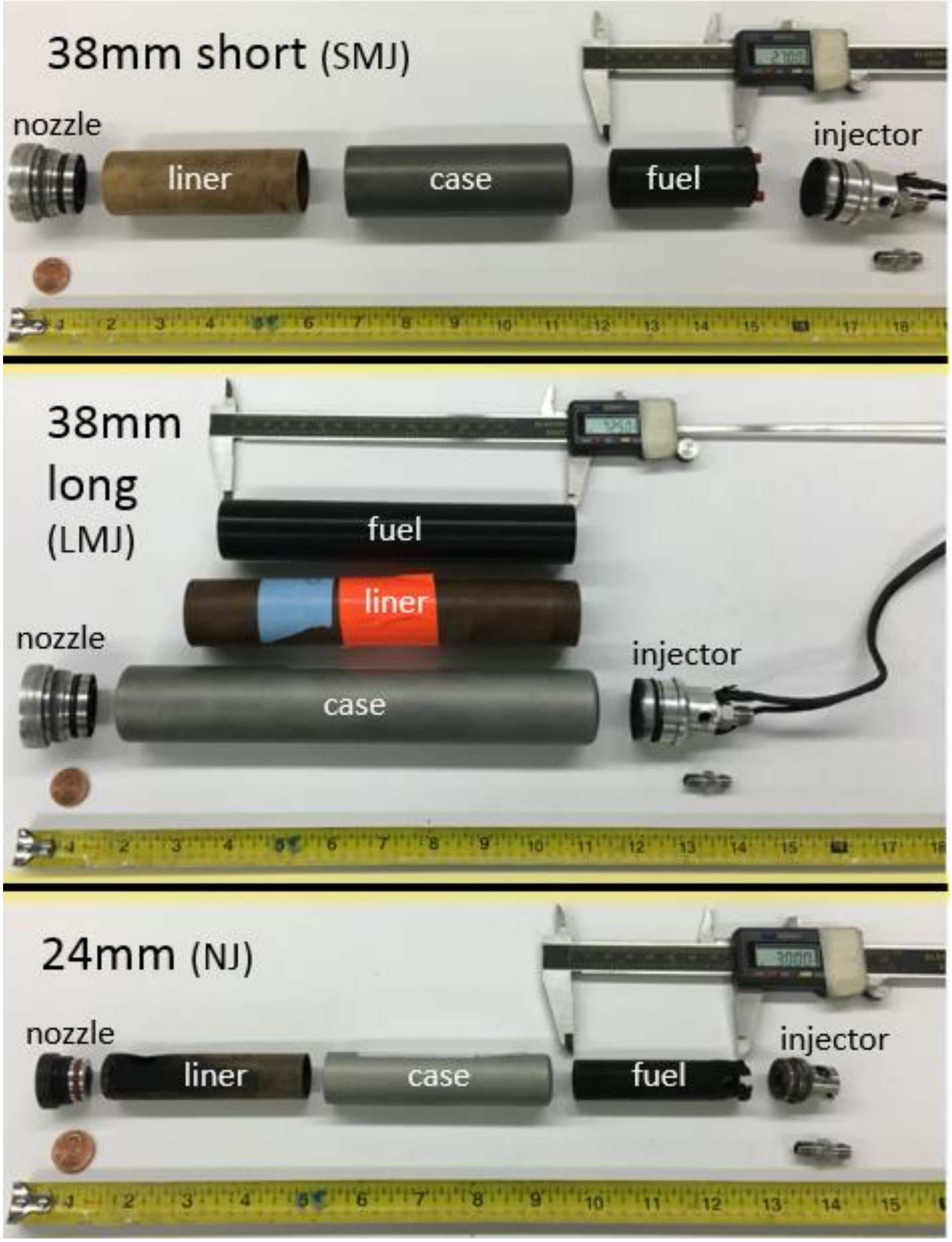

Figure 3.2: Motor Layout for SMJ, LMJ, and NJ

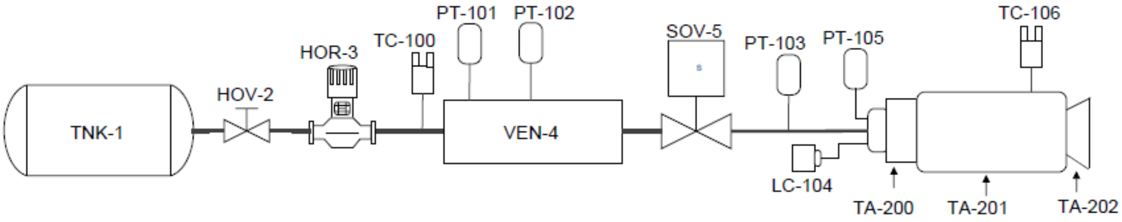

GOX Components	Functional Description
TNK-1	GOX supply tank (2000psi)
HOV-2	GOX supply on/off hand-operated valve
HOR-3	GOX hand-operated pressure reducing regulator
VEN-4	GOX Venturi flow meter
SOV-5	GOX solenoid run valve

Test Article	Functional Description
TA-200	GOX injector cap
TA-201	Motor case
TA-202	Nozzle cap

Sensors	Functional Description
TC-100	Venturi inlet temperature
PT-101	Venturi inlet pressure
PT-102	Venturi differential pressure
PT-103	GOX injector pressure
LC-104	Thrust stand load cell
PT-105	Combustion chamber pressure
TC-106	Motor case temperature

Acronyms
- TNK: tank
- HOV: hand-operated valve
- HOR: hand-operated regulator
- VEN: Venturi flow meter
- SOV: solenoid valve
- TA: test article
- TC: thermocouple
- PT: pressure transducer
- LC: load cell

Figure 3.3: Piping and Instrumentation Diagram

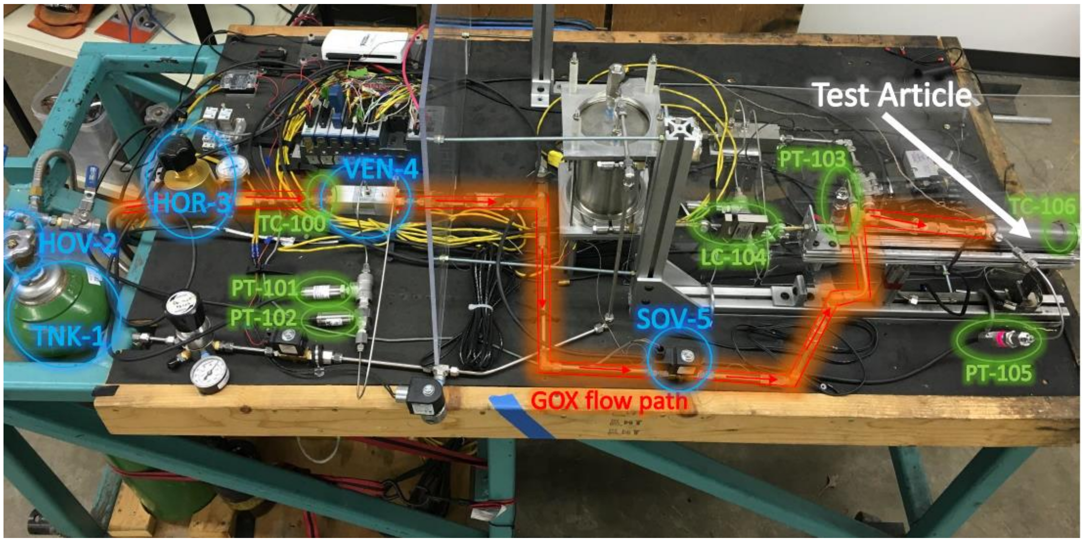

Figure 3.4: Static-Fire Test Stand at Utah State University

CHAPTER IV

RESULTS AND DISCUSSIONS

4.1 Ballistics Model Results

Three small-scale ABS/GOX motor configurations were tested – 1) a 24-mm diameter motor, 2) a low length-to-diameter (L/D) ratio motor with a 38-mm diameter (referred to as S38mm for “short” 38 mm), 3) and a larger length-to-diameter ratio motor also with a 38-mm diameter (called L38mm for “long” 38 mm). For each motor configuration, the ballistics model used parameters of skin friction coefficient scale factor, optical emissivity, empirical scale factor, and burn exponent (τ, ϵ, a, and n', respectively) that minimized the deviation of simulated values from measured values, including fuel mass consumption (amount of fuel mass used during the course motor operation), fuel port diameter expansion, and combustion chamber pressure. In addition, the adjustable parameters were chosen in order to maximize the correlation coefficient and coefficient of determination between the measured and simulated combustion chamber pressure (P_0) – demonstrating the strength of the linear association between measured and simulated values throughout the profile. The final criteria towards the choice of τ, ϵ, a, and n' was algorithm stability, which is governed by the stability of the O/F ratio. Table 4.1 summarizes the criteria used to validate the fuel regression rate models given the adjustable parameters.

The classical Marxman model implemented the same value of skin friction coefficient scale factor (τ) as the augmented Marxman model to give a direct comparison between the two enthalpy-balance models, and the low-fidelity regression rate model (eq.

2.2) implemented a constant empirical scale factor (a) and burn exponent (n') for each motor configuration – ultimately used to compare against hybrid rocket motor studies conducted on different propellant combinations. The values of τ, ϵ, a, and n' that optimized the criteria shown in Table 4.1 are displayed in Fig. 4.1 as a function of motor configuration and then summarized in Tables 4.2 and 4.3.

Table 4.1: Summary of Adjustable Parameters to Optimize Based on Criteria for Ballistics Model Validation

Regression Rate Model	Adjustable Parameters	Criteria to Optimize	Criteria Description
Aug. Marxman	ϵ	Fuel mass consumed	$\%m_{f_{err}} = 100\left(\frac{\lvert m_{f_{measured}} - m_{f_{simulated}}\rvert}{m_{f_{measured}}}\right)$
	τ	Fuel port diameter expansion	$\%D_{p_{err}} = 100\left(\frac{\lvert D_{p_{measured}} - D_{p_{simulated}}\rvert}{D_{p_{measured}}}\right)$
Classic Marxman		Combustion chamber pressure	$\%P_{0_{err}} = 100\left(\frac{\lvert P_{0_{measured}} - P_{0_{simulated}}\rvert}{P_{0_{measured}}}\right)$
Exp. Curve Fit	a	Chamber pressure profile trend	Correlation Coefficient and Coefficient of Determination
	n'	Algorithm stability	Adjustment of parameters such that O/F ratio remains stable

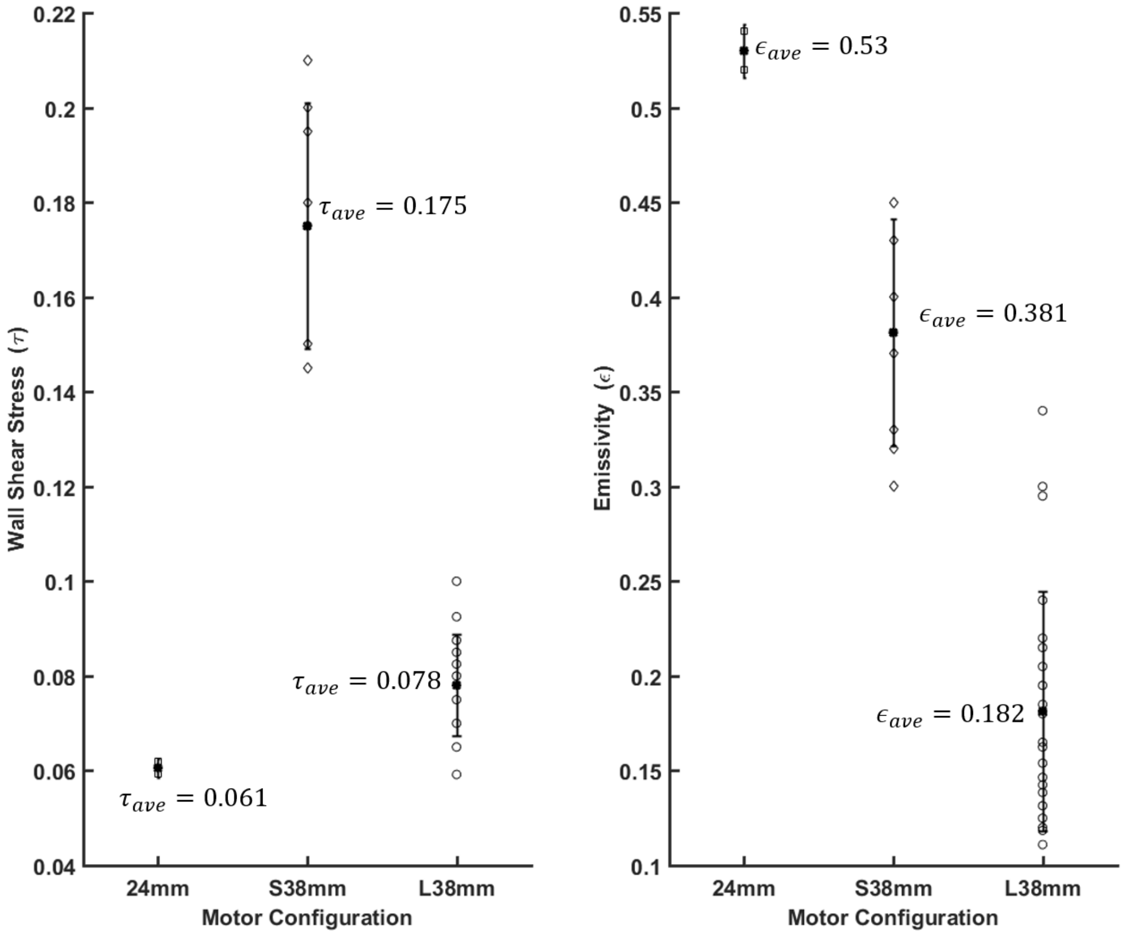

Figure 4.1: Average Wall Shear Stress and Optical Emissivity with Error Bars Representing One Standard Deviation per Motor Configuration

Table 4.2: Summary of Average Adjusted Parameters Within a Student-t 95% Confidence Level per Motor Configuration

Motor	No. of Tests (Sample Size)	$\bar{x} - \frac{t_{\frac{c}{2},\nu}\sigma}{\sqrt{n}} \le \tau_{ave} \le \bar{x} + \frac{t_{\frac{c}{2},\nu}\sigma}{\sqrt{n}}$	$\bar{x} - \frac{t_{\frac{c}{2},\nu}\sigma}{\sqrt{n}} \le \epsilon_{ave} \le \bar{x} + \frac{t_{\frac{c}{2},\nu}\sigma}{\sqrt{n}}$
24mm	2	0.0428 < **0.061** < 0.0784	0.402 < **0.530** < 0.657
S38mm	8	0.1533 < **0.175** < 0.1967	0.331 < **0.381** < 0.431
L38mm	23	0.0734 < **0.078** < 0.0827	0.154 < **0.182** < 0.208

Table 4.3: Exponential Curve Fit Empirical Values per Motor Configuration

Motor	$a\ 1e^{-4}$ (m/s, kg/m^2-s)	n'
24mm	7	0.20
S38mm	6.75	0.22
L38mm	3.5	0.22

Using the values of wall shear stress, optical emissivity, empirical scale factor, and burn exponent per Figure 4.1 and Tables 4.2 and 4.3, the ballistics models produced the following measured-to-simulated fuel mass consumption and port diameter expansion deviation errors (expressed as a percentage) displayed in Fig. 4.2 and summarized in Table 4.4. The resulting errors are rather spread – some high and some low – depending on the implemented regression rate model and motor configuration. The proposed augmented radiation-corrected Marxman model matches fuel mass consumption and port diameter expansion within reasonable percentages (2-10% deviation) with the exception of the smaller length-to-diameter (L/D) ratio motor configuration (S38mm) – actually being described more accurately via the classic Marxman model instead. The cause of this trade-off in regression rate model accuracy may very well be an artifact of motor L/D ratio, which is near unity regarding the S38mm configuration as opposed to the L/D ratio of the 24mm and L38mm motor configurations – having a more standard L/D ratio between 3 and 5. But this discussion will be postponed until the remainder of the statistical analysis is presented.

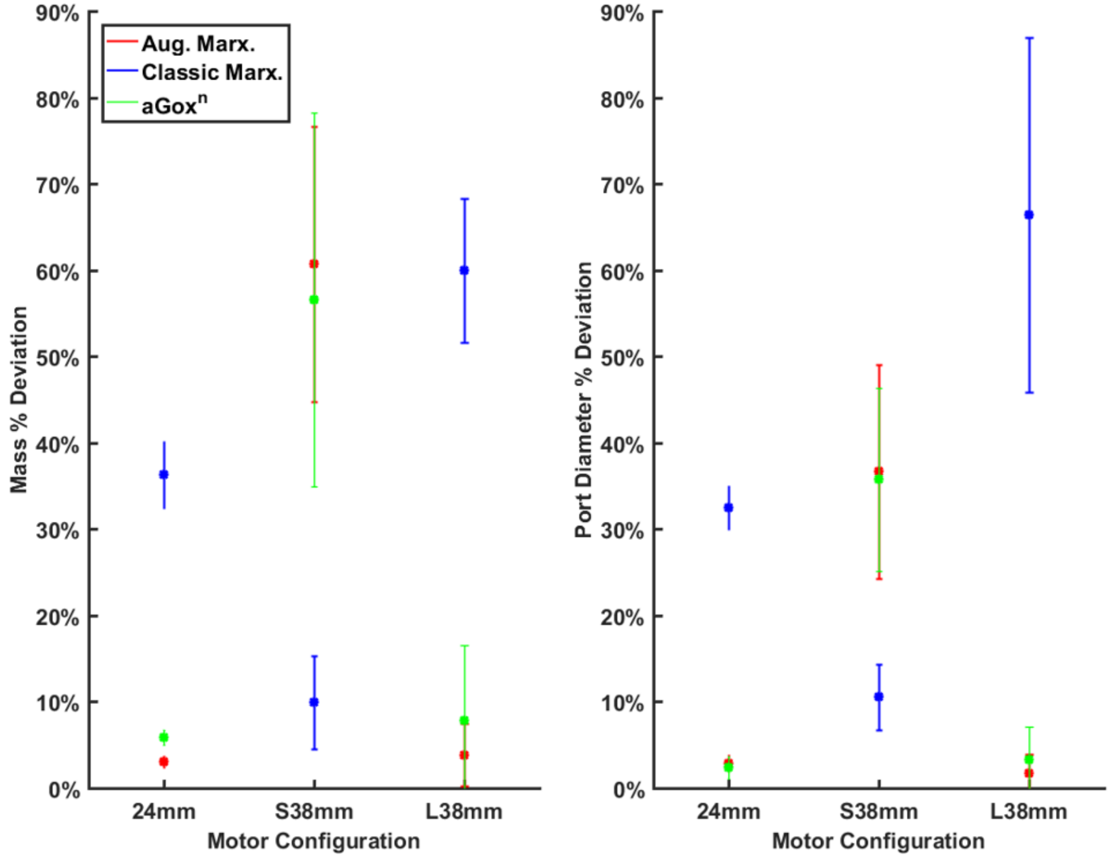

Figure 4.2: Average Measured-to-Simulated Percent Mass and Port Diameter Deviation with Error Bars Representing One Standard Deviation per Regression Rate Model and Motor Configuration

Despite the unusual contrast in the accuracy between regression rate models and motor configurations when regarding fuel mass loss and port diameter expansion, the augmented Marxman model predicts the measured chamber pressure values, as well as the chamber pressure burn profiles accurately for all three motor configurations, including the low L/D ratio motor (S38mm). Figure 4.3 shows a single chamber pressure burn profile for each motor configuration out of the 33 tests to demonstrate the prediction accuracy quantitatively – the other tests vary in burn duration and chamber pressure, but display equivalent chamber pressure prediction accuracies for all three tested motor configurations. Figure 4.3 includes four curves, including the measured chamber pressure data and the simulated data via the augmented Marxman model, the classical Marxman model, and the exponential curve fit model.

Table 4.4: Summary of Average Percent Mass and Port Diameter Deviation Errors within a Student-t 95% Confidence Level per Regression Rate Model and Motor Configuration

Model		**Augmented Marxman**	
Average with Student-t 95% CL		$\%m_{f_{err}}$	$\%D_{p_{err}}$
Motor Config.	24mm	0 < **3.06** < 8.59	0 < **2.87** < 11.19
	S38mm	47.35 < **60.71** < 74.07	26.34 < **36.69** < 47.04
	L38mm	2.25 < **3.82** < 5.39	0.76 < **1.72** < 2.68
Model		**Classical Marxman**	
Average with Student-t 95% CL		$\%m_{f_{err}}$	$\%D_{p_{err}}$
Motor Config.	24mm	2.26 < **36.32** < 70.37	10.31 < **32.48** < 54.65
	S38mm	5.45 < **9.95** < 14.44	7.42 < **10.58** < 13.74
	L38mm	56.33 < **59.97** < 65.56	57.50 < **66.40** < 72.29
Model		**Exponential Curve Fit**	
Average with Student-t 95% CL		$\%m_{f_{err}}$	$\%D_{p_{err}}$
Motor Config.	24mm	0 < **5.87** < 13.81	0 < **2.39** < 13.76
	S38mm	38.47 < **56.57** < 74.66	26.92 < **35.77** < 44.62
	L38mm	4.05 < **7.83** < 11.61	1.67 < **3.30** < 4.93

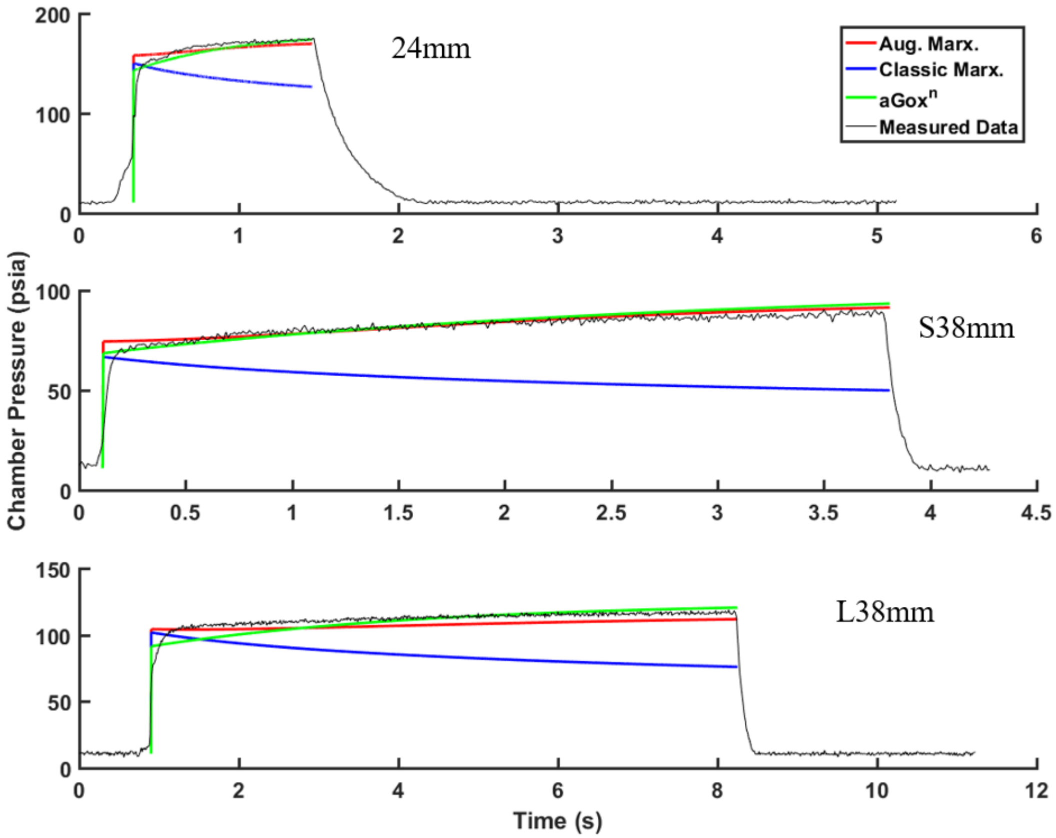

Figure 4.3: Comparison of Measured Chamber Pressure to Simulated Chamber Pressure Using Varying Ballistics Models for Small-Scale ABS/GOX Hybrid Rocket Motors

It is evident that the classical Marxman model under-predicts the measured chamber pressure and describes the chamber pressure trend inaccurately with a steady-state chamber pressure that drops as a function of burn time instead of increase, as the augmented Marxman model does. To assess the entire set of tests, the average RMSE percentage of measured-to-simulated chamber pressure is displayed as a function of fuel port diameter ratio (defined as the ratio of current port diameter to initial port diameter) for all 33 tests. This is displayed in Fig. 4.4, where the average RMSE percentage measured across all tests for a given port diameter ratio is plotted with each corresponding error bar, representing one standard deviation.

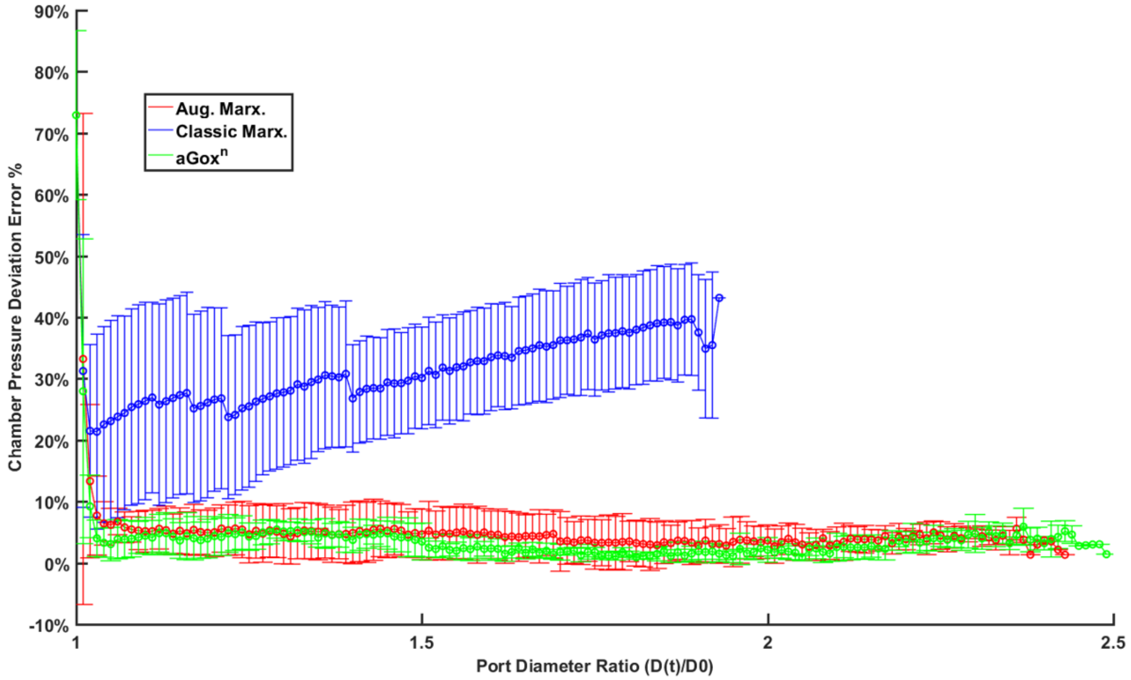

Figure 4.4: Measured-to-Simulated Chamber Pressure RMSE Percentage as a Function of Port Diameter Ratio Encompassing All Tests

As the fuel port diameter expands, the simulated chamber pressure via the augmented Marxman and exponential curve fit models – using the parameters per Fig. 4.1 and Tables 4.2 and 4.3 – estimate the measured chamber pressure values within 90-100% accuracy. Whereas the classical Marxman model predicts within approximately 60-80% accuracy and becomes progressively worse as a function of port diameter expansion due to incorrectly predicting the measured chamber pressure profile. Additionally, Fig. 4.4 further demonstrates how the classical Marxman model under-predicts small-scale

ABS/GOX hybrid rocket fuel regression rates since the simulated port diameter expansion only goes up to about a ratio of 2 instead of 2.5. The large initial errors shown in Fig. 4.4 are due to the inability to simulate the transient start-up of HRMs in general, which is a more involved process to characterize. However, steady-state behavior is achieved within the first few milliseconds of motor operation. Figure 4.5 illustrates the difference in measured-to-simulated chamber pressure accuracy when capturing the full burn profile and when capturing the steady-state burn profile – displaying the average simulated chamber pressure RMSE percentage, correlation coefficient, and coefficient of determination that encompasses all 33 tests.

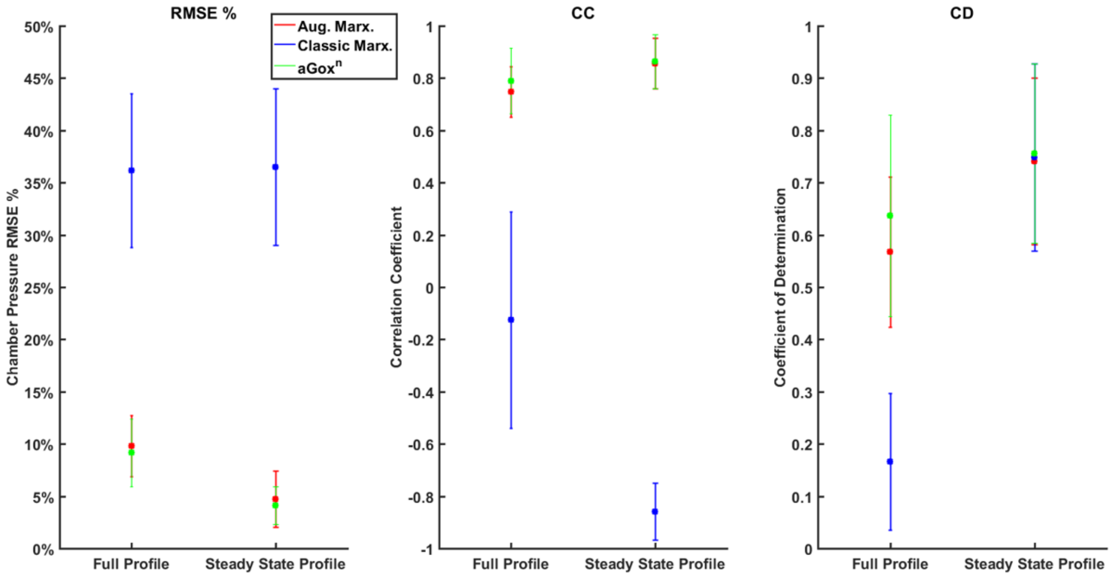

Figure 4.5: Average Chamber Pressure RMSE Percent, Correlation Coefficient, and Coefficient of Determination Across All Test Data

The measured-to-simulated chamber pressure RMSE error improves by almost a factor of 2 when excluding the initial transient conditions using the augmented Marxman and exponential curve fit models to predict chamber pressure for ABS/GOX hybrids. The predictions accomplished through the classical Marxman model maintain the same level of error, but reveal an interesting value of the correlation coefficient, which is near -1. This means that the steady-state chamber pressure profile simulated through the classical Marxman model has a strong negative linear correlation to the measured chamber pressure data – implying that as measured chamber pressure increases, the simulated chamber pressure decreases in a manner that is nearly linear. The augmented Marxman and exponential curve fit models, on the other hand, simulate chamber pressure with a strong positive linear correlation to the measured chamber pressure (correlation coefficient is near +1).

Through the coefficient of determination, which is approximately between 65-85%, it can be concluded that about 75% of the variation in the measured chamber pressure data can be justified by the linear relationship between the simulated and measured chamber pressure (the simulated chamber pressure data through the classical Marxman model can also explain 75% of the variation, but for a negative linear correlation). As such, the radiation-corrected regression rate can describe the behavior of chamber pressure as a function of burn duration, whereas the convection-only regression rate describes an opposite behavior. This also further establishes the empirical scale factor and burn exponents used to match small-scale motor, ABS/GOX propellant combination. The results shown in Fig. 4.5 are summarized in Table 4.5.

Table 4.5: Summary of Average Chamber Pressure RMSE %, Correlation Coefficient, and Coefficient of Determination within a Student-t 95% Confidence Level per Regression Rate Model and Burn Profile Section

Model		**Augmented Marxman**		
Average with Student-t 95% CL		P_0 RSME %	CC	CD
Profile	Full	8.77 < **9.81** < 10.84	0.71 < **0.75** < 0.78	0.51 < **0.57** < 0.61
	Steady State	3.77 < **4.72** < 5.67	0.82 < **0.86** < 0.89	0.68 < **0.74** < 0.79
Model		**Classical Marxman**		
Average with Student-t 95% CL		P_0 RSME %	CC	CD
Profile	Full	33.56 < **37.37** < 38.77	-0.27 < **-0.12** < 0.02	0.12 < **0.16** < 0.21
	Steady State	33.84 < **38.38** < 39.14	-0.89 < **-0.86** < -0.82	0.68 < **0.75** < 0.81
Model		**Augmented Marxman**		
Average with Student-t 95% CL		P_0 RSME %	CC	CD
Profile	Full	8.03 < **9.17** < 10.32	0.74 < **0.79** < 0.83	0.56 < **0.64** < 0.70
	Steady State	3.48 < **4.32** < 4.75	0.82 < **0.86** < 0.90	0.69 < **0.76** < 0.81

The augmented radiation-corrected Marxman model has demonstrated the ability to meet the criteria of predicting measured fuel mass consumption, port diameter expansion, and chamber pressure more accurately than the original convection-only Marxman model regarding ABS/GOX hybrid rocket motor performance. The one exception to this was in predicting the fuel mass loss and port diameter expansion for the small L/D ratio motor (S38mm), where the augmented Marxman model over-predicted by up to 80% and the classic Marxman model predicted within 10% deviation error. Despite this, the augmented Marxman model predicts measured chamber pressure very accurately across all motor configurations where the classical Marxman model does not, including the small L/D ratio motor. This indicates that the S38mm motor operates within a "grey" region between the classical and augmented Marxman models, where one model describes a certain parameter better than the other but fails at describing another parameter. Table 4.6 summarizes the L/D ratios of the three motor configurations tested.

Table 4.6: Length-to-Diameter Ratios of Tested Motor Configurations

Motor	Length (cm)	Diameter (cm)	L/D Ratio
24mm	7.645	2.4	3.19
S38mm	6.812	3.8	1.79
L38mm	18.415	3.8	4.85

Table 4.6 suggests that hybrid rocket motors with L/D ratios closer to unity operate with combustion physics that are not fully captured by either the classical nor augmented Marxman models. This may be due to insufficient fuel particle accumulation within the combustion chamber since it has less length to travel before exiting the nozzle. As such, radiative effects are still apparent but the motor length is not long enough to ablate additional fuel via particle accumulation bombardment. An investigation into near-unity L/D ratio motors will be reserved for future studies.

4.2 Discussion of Results

In conclusion of the ballistics model validation, the success of the augmented radiation-corrected Marxman model, as described in Eqs. 2.23-2.29, demonstrates the relevance of including radiative energy transfer – producing simulated parameters that closely match experimentally-obtained parameters for small-scale ABS/GOX hybrid rocket motors where chamber pressure was the primary criteria of optimization. Examining the O/F ratio shift using the augmented Marxman fuel regression rate model:

$$O/F = \frac{\dot{m}_{ox}}{\dot{m}_f} = \frac{G_{ox} D_p}{4 \rho_f L \dot{r}} \tag{4.1}$$

$$O/F = \frac{G_{ox} D_p}{4 \rho_f L \left(\frac{0.635 \tau G_{ox}^{n}}{n \rho_f P_r^{\frac{2}{3}}} \left(\frac{\Delta h}{h_v}\right) \left(\frac{\mu}{L}\right)^{1-n} \left(\frac{1}{\beta^{0.77}}\right) + \frac{\sigma\left(\epsilon T_0^4 - \alpha T_f^4\right)}{\rho_f h_v} \right)} \tag{4.2}$$

$$O/F = \frac{1}{\left(D_p^{1-2^n} \left(\frac{2.54 L \tau}{n P_r^{\frac{2}{3}}} \right) \left(\frac{\Delta h}{h_v}\right) \left(\frac{1}{\beta^{0.77}}\right) \left(\frac{\mu}{L}\right)^{1-n} \left(\frac{4 \dot{m}_{ox}}{\pi}\right)^{n-1} + \frac{\pi D_p L}{\dot{m}_{ox}} \left(\frac{\sigma\left(\epsilon T_0^4 - \alpha T_f^4\right)}{h_v} \right) \right)} \tag{4.3}$$

Quantitative examination of equation 4.3 shows that for Marxman exponent values of $n > \frac{1}{2}$, the convective term becomes fuel-leaner with time as port diameter grows and the radiative term becomes fuel-richer with time as port diameter grows. For

$n < \frac{1}{2}$, both the convective and radiative terms become fuel-richer with time as port diameter grows. Since the Marxman exponent of $n = 0.8$ remained unchanged throughout this study, the O/F ratio contribution towards increasingly fuel-rich tendencies was due to the radiative energy transfer term – the original postulation that brought about this research. Similarly, upon examination of the ratio between the radiative and convective terms,

$$\frac{\dot{r}_{radiation}}{\dot{r}_{convection}} = \frac{\dfrac{\sigma\left(\epsilon T_0^4 - \alpha T_f^4\right)}{\rho_f h_v}}{\dfrac{0.635\tau G_{ox}^n}{n\rho_f P_r^{\frac{2}{3}}}\left(\dfrac{\Delta h}{h_v}\right)\left(\dfrac{\mu}{L}\right)^{1-n}\left(\dfrac{1}{\beta^{0.77}}\right)} \tag{4.4}$$

$$\frac{\dot{r}_{radiation}}{\dot{r}_{convection}} = \left(\frac{1}{G_{ox}^n}\right)\left(\frac{\dfrac{\sigma\left(\epsilon T_0^4 - \alpha T_f^4\right)}{h_v}}{\dfrac{0.635\tau}{nP_r^{\frac{2}{3}}}\left(\dfrac{\Delta h}{h_v}\right)\left(\dfrac{\mu}{L}\right)^{1-n}\left(\dfrac{1}{\beta^{0.77}}\right)}\right) \tag{4.5}$$

Quantitative analysis of Eq. 4.5 suggests that at low oxidizer mass flux levels, the radiation term dominates – tending towards a fuel-rich burn. At high oxidizer mass flux levels, the convection term dominates – tending towards a fuel-lean burn. This predicts the contradictory result between the O/F ratio shifts between small-scale ABS/GOX HRMs and HRMs using different propellants at higher oxidizer mass fluxes as shown in Fig. 2.4. As such, the low burn exponents can be explained as a result of non-negligible radiative energy transfer.

CHAPTER V

CONCLUSIONS

Utah State University has conducted extensive research on hybrid rocket motors (HRM) using additively-manufactured acrylonitrile butadiene styrene (ABS) as a fuel – granting access to convenient HRM geometry scaling. Various medium to small-scale motors have been tested, including 98, 75, 54, 38, and 24 mm diameter motor configurations. In addition to scalability, additively-manufactured ABS serves as a benign, non-toxic, and low-cost fuel source. Previous studies at Utah State University revealed that ABS performance matches hydroxyl-terminated polybutadiene (HTPB) as a propellant, has superior structural properties, and exhibits a certain level of electrical conductivity, which can be exploited to serve as an ignition source. This patent-pending arc-ignition technology developed at Utah State University requires very brief and minimal power levels – allowing for a rapid and high fidelity restartable propulsion system.

Through the continuing technology readiness level (TRL) development, ABS as a hybrid rocket fuel is receiving increasing attention as a feasible small-spacecraft propulsion system – initiating an involved research campaign in order to characterize small-scale ABS hybrid rocket motor performance. Using ABS fuel and gaseous oxygen (GOX) as an oxidizer, a relatively low stoichiometric oxidizer-to-fuel (O/F) ratio has been determined. Furthermore, ABS/GOX hybrid rocket motors exhibit an O/F ratio shift that decreases as the fuel port diameter expands. This implies that the O/F ratio becomes more fuel-rich during the operation of ABS/GOX HRMs, and has been quantitatively observed in the form of a transient, bright-to-sooty exhaust plume – directly contrasting the standard O/F ratio shift seen in other hybrid rocket propellant combinations, which become more oxidizer-rich with time. In addition to the fuel-rich tendencies of ABS/GOX propellant combinations, the magnitude of the fuel-rich O/F shift increases as the motor scale decreases – suggesting that this contradictory behavior is further due to the small-scale motor sizes, which were only recently achievable through additive-manufacturing techniques. Considering ABS/GOX propellant combinations, small-scale motors, and the relatively lower oxidizer mass flux levels associated with small-scale motors, a radiative energy transfer mechanism – normally considered negligible – is reintroduced and studied; the postulation being that radiative energy transfer becomes the dominant source of fuel regression rates, which in turn increase the amount of fuel mass flow and thus decrease the O/F ratio.

After modifying the enthalpy-balance-based classical Marxman model to account for radiative energy transfer, an augmented Marxman model was developed and tested against a substantial database of measured values, including fuel mass consumption, port diameter expansion, and combustion chamber pressure. Simulated values via the augmented ballistics model demonstrate an accuracy between 85-100% agreement with the experimental data, whereas the ballistics model implementing the classical Marxman model agree within 20-60%. Based on the level of agreement between the simulated-to-measured values regarding the augmented Marxman model, the scale factor and burn exponent for the empirically-based fuel regression rate have been determined – revealing burn exponent values less than 0.5 for medium to small-scale ABS/GOX HRMs.

Furthermore, the burn exponent deviates increasingly lower from 0.5 as the motor diameter decreases – demonstrating a progressively more aggressive fuel-rich O/F ratio shift. Since other HRM propellant combinations such as HTPB with nitrous oxide (N_2O) and Paraffin wax with liquid oxygen (LOX) exhibit burn exponents whose values are greater than 0.5, which describe fuel-lean O/F ratio shifts, the contradictory behavior between ABS/GOX and other HRM propellant combinations have been observed and described both qualitatively and quantitatively.

Through this analysis, the postulation of a dominant radiative energy transfer mechanism maintains a certain level of merit (not considered absolutely true, but pointing in the right direction), and may explain the majority of the contradictory O/F ratio shift behavior observed in medium to small-scale ABS/GOX hybrid rocket motors.

CHAPTER VI

FUTURE WORK

The study conducted within the scope of this thesis reveals that radiative energy transfer accounts for a large portion of the combustion behavior regarding small-scale, ABS-fueled hybrid rocket motors. However, some ambiguity exists about what exactly causes the behavior, or, if it is a combination of certain parameters, how much each parameter contributes to the behavior. A good example of this uncertainty is seen in the low length-to-diameter (L/D) ratio motor that was tested: demonstrating that the classic Marxman model accurately predicted experimentally-measured fuel mass loss and port diameter expansion but, on the other hand, inaccurately under-predicted experimentally-measured chamber pressure as well as inaccurately describe the chamber pressure and O/F ratio shift. The augmented Marxman model produced opposite results – over-predicting measured fuel mass loss and port diameter expansion, but accurately predicting measured chamber pressure values, shift, and O/F ratio shift. This tradeoff suggests that the low L/D ratio motor is still largely affected by radiative energy transfer effects, but does not regress as much fuel as the radiation-corrected regression rate model predicts, which is challenging to predict theoretically because it poses somewhat of a paradox.

By implementing the augmented Marxman model with a strong optical emissivity, the fuel regression rate is amplified. This produces a larger mass flow rate, which produces a larger chamber pressure and smaller O/F ratio, but also results in larger fuel mass loss and port diameter expansion. Although this described the experimentally-measured values of the higher L/D ratio motors all around, the smaller L/D ratio motor gained too much fuel mass loss and port diameter expansion as described by the augmented Marxman model. If the augmented Marxman model is implemented with a weak optical emissivity, the fuel regression rate is lower and dominated more so by convective energy transfer mechanisms. The result is an O/F ratio that is over-predicted, chamber pressure that is under-predicted, and a predicted fuel mass loss and port diameter expansion that is fairly accurate. As the model currently stands, the best compromise between the two cases would result in a chamber pressure predicted at about 25% less than the measured value and a fuel mass loss and port diameter expansion predicted at about 50% more than the measured value – based on the analysis conducted in this thesis. This is not a satisfactory result and requires a different approach towards the manipulation of the enthalpy-balance derivation – likely something involving the motor length since the primary difference between the studied small-scale motors is the L/D ratio, where motor diameters were similar.

Despite the ambiguity regarding the L/D ratios, it seems evident that motor scale effects contribute to the radiative energy transfer effects, at least to some degree. However, it is still unknown if this is a phenomenon unique to additively-manufactured ABS, or if radiative energy transfer mechanisms are a fundamental property inherent to all small-scale hybrid rocket motors – regardless of propellant combination. The magnitude of the oxidizer mass flow is also questionable because the fuel-rich properties may simply be an artifact of using minimal oxidizer mass-flow levels.

Future studies should investigate the effects of the L/D ratio by testing with a suite of motors with equivalent diameters but varying lengths, and should test these motors at varying oxidizer flow rates. Additionally, tests should be conducted using multiple fuels including ABS, ABS with different constituent percentages, ABS printed in varying colors, paraffin mixtures, HTPB, HDPE, and LDPE mixtures. This would call for a highly-involved testing campaign, but would potentially demystify the unusual behavior of small-scale, ABS-fueled HRMs and prove or disprove that all small-scale HRMs, regardless of propellant combination, operate within a radiation-dominant combustion regime – exhibiting fuel-rich tendencies.

REFERENCES

[1] Giovanni Verlini, “The Bright Future of Small Satellite Technology,” Via Satellite, August 1, 2011, http://www.satellitetoday.com/publications/via-satellite-magazine/features/2011/08/01/the-bright-future-of-small-satellite-technology/, [Retrieved 04 October, 2016].

[2] Conor O’Sullivan, “IGS Low Cost Access to Space,” Catapult Satellite Applications, April 2016, http://www.slideapp.net/igs-low-cost-access-to-space-april-2016, [Retrieved 04 October, 2016].

[3] Inter-Agency Space Debris Coordination Committee, “IADC Space Debris Mitigation Guidelines,” IADC-02-01, Revision 1, September 2007, http://www.unoosa.org/documents/pdf/spacelaw/sd/IADC-2002-01-IADC-Space_Debris-Guidelines-Revision1.pdf, [Retrieved 04 October, 2016].

[4] Anon., “Hazard Analysis of Commercial Space Transportation; Vol. 1: Operations, Vol. 2: Hazards, Vol. 3: Risk Analysis,” U.S. Dept. of Transportation, PB93-199040, Accession No. 00620693, May 1988.

[5] Stephen A. Whitmore, Sean D. Walker, Daniel P. Merkley, and Mansour Sobbi. "High Regression Rate Hybrid Rocket Fuel Grains with Helical Port Structures", *AIAA J. Propulsion and Power*, Vol. 31, No. 6 (2015), pp. 1727-1738.

[6] Kuo, K. K. and Chiaverini, M. J., *Fundamentals of Hybrid Rocket Combustion and Propulsion, Progress in Astronautics and Aeronautics,* AIAA, Reston, VA, 2007, Chap. 7.

[7] Stephen A. Whitmore. "Additively Manufactured Acrylonitrile-Butadiene-Styrene–Nitrous-Oxide Hybrid Rocket Motor with Electrostatic Igniter", *AIAA J. Propulsion and Power* r, Vol. 31, No. 4 (2015), pp. 1217-1220.

[8] Wikipedia the Free Encyclopedia, “Fused deposition modeling,” Wikipedia, https://en.wikipedia.org/wiki/Fused_deposition_modeling, [Retrieved 04 October, 2016].

[9] Stephen A. Whitmore, Nathan Inkley, and Daniel P. Merkley, "Development of a Power-Efficient, Restart-Capable Arc Ignitor for Hybrid Rockets", *AIAA J. Propulsion and Power*, Vol. 31, No. 6 (2015), pp. 1739-1749.

[10] Stephen A. Whitmore and Stephen L. Merkley. “Effects of Radiation Heating on Additively Printed Hybrid Fuel Grain O/F Shift”, 52nd AIAA/SAE/ASEE Joint Propulsion Conference, AIAA Propulsion and Energy Forum, (AIAA 2016-4867).

[11] Whitmore, Stephen A., Peterson, Zachary W., and Eilers, Shannon D., “Comparing Hydroxyl Terminated Polybutadiene and Acrylonitrile Butadiene Styrene as Hybrid Rocket Fuels,” *AIAA J. Propulsion and Power*, vol. 29, no. 3, May-June 2013.

[12] Arif M. Karabeyoglu and Brian J. Evans. "Effect of O/F Shift on Combustion Efficiency," 50th AIAA/ASME/SAE/ASEE Joint Propulsion Conference, AIAA Propulsion and Energy Forum, (AIAA 2014-3851).

[13] Greg Zilliac and M. Arif Karabeyoglu, "Hybrid Rocket Fuel Regression Rate Data and Modeling," *AIAA J. Propulsion and Power July 2006*, AIAA 2006-4504.

[14] Marxman, G. and M.Gilbert, "Turbulent boundary layer combustion in the hybrid rocket," *Symposium (International) on Combustion*, Vol. 9, No. 1., 1963, pp. 371–383.

[15] Brian Cantwell, "Aircraft and Rocket Propulsion Chapter 11," AA 283 Hybrid Rockets, AAE Department Stanford University, May 2012, http://web.stanford.edu/~cantwell/AA283_Course_Material/AA283_Ch_11_Hybrid_Rockets.pdf, [Retrieved 04 October, 2016].

[16] George P. Sutton and Oscar Biblarz, "Rocket Propulsion Elements," John Willey and Sons Inc., 8th Ed., 2010, chp. 15.

[17] Whitmore, Stephen A., Peterson, Zachary W., and Eilers, Shannon D., "Comparing Hydroxyl Terminated Polybutadiene and Acrylonitrile Butadiene Styrene as Hybrid Rocket Fuels," *AIAA J. Propulsion and Power*, vol. 29, no. 3, May–June 2013.

[18] Lees, L., "Convective Heat Transfer with Mass Addition and Chemical Reactions," *Combustion and Propulsion, 3rd AGARD Colloquium*, New York, Pergamon Press, 1958, p. 451.

[19] White, Frank M., *Viscous Fluid Flow*, McGrawHill, Inc., New York, 1991, pp. 485-486.

[20] CFD Online, "Skin friction coefficient," CFD Online, http://www.cfd-online.com/Wiki/Skin_friction_coefficient, [Retrieved 04 October, 2016].

[21] Arif Karabeyoglu, "Lecture 10 Hybrid Rocket propulsion Design Issues," AA 284a Advanced Rocket Propulsion, AAE Department, Stanford University, May 14, 2012, p. 18, http://www.spg-corp.com/docs/Stanford_AA284a_Lecture10.pdf, [Retrieved 01 January, 2016].